

Deep Regularized Compound Gaussian Network for Solving Linear Inverse Problems

Carter Lyons^{1,2}, Raghu G. Raj¹, and Margaret Cheney²

¹U.S. Naval Research Laboratory, Washington, D.C.

²Colorado State University, Fort Collins, CO

Abstract—Incorporating prior information into inverse problems, e.g. via maximum-a-posteriori estimation, is an important technique for facilitating robust inverse problem solutions. In this paper, we devise two novel approaches for linear inverse problems that permit problem-specific statistical prior selections within the compound Gaussian (CG) class of distributions. The CG class subsumes many commonly used priors in signal and image reconstruction methods including those of sparsity-based approaches. The first method developed is an iterative algorithm, called generalized compound Gaussian least squares (G-CG-LS), that minimizes a regularized least squares objective function where the regularization enforces a CG prior. G-CG-LS is then unrolled, or unfolded, to furnish our second method, which is a novel deep regularized (DR) neural network, called DR-CG-Net, that learns the prior information. A detailed computational theory on convergence properties of G-CG-LS and thorough numerical experiments for DR-CG-Net are provided. Due to the comprehensive nature of the CG prior, these experiments show that DR-CG-Net outperforms competitive prior art methods in tomographic imaging and compressive sensing, especially in challenging low-training scenarios.

Index Terms—Machine learning, deep neural networks, inverse problems, nonlinear programming, least squares methods

I. INTRODUCTION

LINEAR inverse problems enjoy extensive applications throughout scientific and engineering disciplines – including X-ray computed tomography, magnetic resonance imaging (MRI), radar imaging, sonar imaging, and compressive sensing (CS) – making it an active area of research.

Until recently, iterative or model-based approaches were the main methodologies to solve (linear) inverse problems and typically incorporate an expected prior density into an estimation algorithm. Example iterative algorithms include the Iterative Shrinkage and Thresholding Algorithm (ISTA) [1, 2], Bayesian Compressive Sensing [3], and Compressive Sampling Matching Pursuit [4, 5]. Many previous works implement a generalized Gaussian prior [1, 2, 5], which is encompassed by the broad compound Gaussian (CG) prior that better captures statistical properties of images [6]–[10].

Innovations in artificial intelligence (AI) and machine learning (ML), particularly deep learning, paired with advance-

ments in computational efficiency, have yielded prominent tools with tremendous applications to signal and image processing problems including inverse problems. Deep learning approaches construct a function mapping between a domain and range of interest by training a deep neural network (DNN), i.e. a NN with a sizeable number of layers, with instantiations of domain-range pairs. For inverse problems, measurement-signal pairs serve as the domain-range pairs used in training. Many previous works use standard DNN methods including convolutional neural networks (CNN), recurrent neural networks, or generative adversarial networks [11]–[16].

Algorithm unrolling or unfolding, stemming from the original work of Gregor and LeCun [17], is a recent approach to inverse problems that combines the model-based and data-driven methods by structuring the layers of a DNN upon an iterative algorithm. While a standard DNN acts as a black-box process, we have some understanding of the inner workings of an unrolled DNN by understanding the original iterative algorithm. Additionally, algorithm unrolling seamlessly allows for the incorporation of a prior density into a deep learning framework. These factors contribute to the success of algorithm unrolled methods, which have shown excellent performance in image estimation while offering interpretability of the network layers [18]. Algorithm unrolling has been applied to many iterative algorithms including ISTA [17]–[21], proximal gradient or gradient descent [22, 23], the inertial proximal algorithm for non-convex optimization [24], and the primal-dual algorithm [25].

A. Contributions

This paper constructs a CG-based iterative signal estimation algorithm and then leverages algorithm unrolling to develop novel DNN structures, for solving linear inverse problems, that are fundamentally informed by a learned CG prior. In particular we:

- 1) Develop a novel CG-based iterative algorithm, called generalized compound Gaussian least squares (G-CG-LS), for linear inverse problems, which reduces to previous CG-based approaches [8] and Tikhonov regularization as special cases. Specifically, G-CG-LS solves a regularized least squares optimization problem with two regularization terms consisting of a Gaussian term and an implicitly defined non-Gaussian term, which together enforce a CG prior.

carter.lyons@colostate.edu
raghu.g.raj@ieee.org
margaret.cheney@colostate.edu

This work was sponsored in part by the Office of Naval Research via the NRL base program and under award number N00014-21-1-2145 and in part by the Air Force Office of Scientific Research under award number FA9550-21-1-0169.

Project codes are accessible at <https://github.com/clyons19/DR-CG-Net>.

- 2) Derive a theoretical convergence analysis for G-CG-LS to stationary points of the underlying cost function to provide insight into the performance of G-CG-LS.
- 3) Construct novel CG-based DNNs, called deep regularized compound Gaussian network (DR-CG-Net), by applying the algorithm unrolling technique to G-CG-LS, such that the implicit portion of the regularization is trainable, thereby allowing for learning of the prior density within the powerful CG class of distributions.
- 4) Present novel empirical results for DR-CG-Net on tomographic imaging and CS problems. We demonstrate the effectiveness of DR-CG-Net when limited to small training datasets and show a significant improvement over other state-of-the-art deep learning-based approaches.

Our proposed G-CG-LS and DR-CG-Net are expansions on prior art CG-based methods [8, 26, 27]. A core novelty of the DR-CG-Net framework, compared to previous CG-based methods, is the ability to learn arbitrary signal priors within the CG distribution class. As such, we generalize to a broader signal prior within the CG-prior context. Furthermore, our proposed methods can be reduced to prior CG-based methods [8, 26, 27] as special cases. Empirically, we demonstrate significant improvement, in estimated signal quality and time, for DR-CG-Net over previous CG-based methods.

II. BACKGROUND

In this section, we provide brief introductions to the CG prior, DNNs, and algorithm unrolling as these are the key components we combine to furnish the methods developed in this paper. First, the linear measurement (i.e. forward) model we consider throughout this paper is

$$\mathbf{y} = \mathbf{A}\mathbf{c} + \boldsymbol{\nu} \quad (1)$$

where $\mathbf{y} \in \mathbb{R}^m$ are the measurements, $\mathbf{A} \in \mathbb{R}^{m \times n}$ is a sensing matrix, $\mathbf{c} \in \mathbb{R}^n$ is the unknown signal, and $\boldsymbol{\nu} \in \mathbb{R}^m$ is additive white noise. In many applications of interest, $m \ll n$ and \mathbf{A} is decomposed as $\mathbf{A} = \Psi\Phi$ for $\Psi \in \mathbb{R}^{m \times n}$ a measurement matrix and $\Phi \in \mathbb{R}^{n \times n}$ a change of basis dictionary. This formulation results from representing an original signal, \mathbf{s} , with respect to (w.r.t.) Φ as $\mathbf{s} = \Phi\mathbf{c}$. Signal reconstruction, or estimation, is the inverse problem of recovering \mathbf{c} , or \mathbf{s} , given \mathbf{y} , Ψ , and Φ .

A. Compound Gaussian Prior

A fruitful way to formulate inverse problems is by Bayesian estimation, in particular, a maximum a posteriori (MAP) estimate. The MAP estimate of \mathbf{c} from (1) depends crucially on the assumed prior density of \mathbf{c} , which serves to incorporate domain-level knowledge into the inverse problem. Many previous works employ a generalized Gaussian prior [6, 7] such as a Gaussian prior for Tikhonov regression [28] or a Laplacian prior as is predominant in the CS framework [1, 2, 4, 5].

Through the study of the statistics of image sparsity coefficients, it has been shown that coefficients of natural images exhibit self-similarity, heavy-tailed marginal distributions, and self-reinforcement among local coefficients [7]. Such properties are not encompassed by the generalized Gaussian prior. Instead, CG densities [29], also known as Gaussian scale

mixtures [6, 7], better capture these statistical properties of natural images and images from other modalities such as radar [9, 10]. A useful formulation of the CG prior lies in modeling a signal \mathbf{c} as the Hadamard product

$$\mathbf{c} = \mathbf{z} \odot \mathbf{u} := [z_1 u_1, z_2 u_2, \dots, z_n u_n]^T \quad (2)$$

such that $\mathbf{u} \sim \mathcal{N}(\mathbf{0}, \Sigma_u)$, $\mathbf{z} \sim p_{\mathbf{z}}$ is a positive random vector, and \mathbf{u} and \mathbf{z} are independent [7, 29]. We call \mathbf{u} and \mathbf{z} as the Gaussian variable and scale variable, respectively. It has been shown in [7, 8] that by suitably defining the distribution of \mathbf{z} , the CG prior subsumes many well-known distributions including the generalized Gaussian, student's t , α -stable, and symmetrized Gamma distributions.

Previously, the CG prior has been used with a log-normal distributed scale variable in an iterative MAP estimate of wavelet and discrete cosine transformation (DCT) image coefficients [29, 30]. Additionally, a log-normal distribution for \mathbf{z} was used in an alternative and simplified iterative MAP estimation of image coefficients that was subsequently unrolled into a DNN [8, 26, 27]. Furthermore, the CG prior using a real-valued random scale variable has been successfully used for image denoising [31] and hyperspectral image CS [32].

B. Deep Neural Networks and Algorithm Unrolling

A DNN is a collection of ordered layers, denoted $\mathbf{L}_0, \mathbf{L}_1, \dots, \mathbf{L}_K$ for $K > 1$, that form a directed acyclic graph starting with the input layer, \mathbf{L}_0 , and ending at the output layer, \mathbf{L}_K . Intermediate layers $\mathbf{L}_1, \dots, \mathbf{L}_{K-1}$ are known as hidden layers. Each layer, \mathbf{L}_k , contains d_k nodes, or hidden units [33], and for simplicity, we identify the nodes with the computed values assigned when a signal is processed by the DNN.

A function $\mathbf{f}_k : \mathbb{R}^{d_{i_1(k)}} \times \dots \times \mathbb{R}^{d_{i_j(k)}} \rightarrow \mathbb{R}^{d_k}$, that is parameterized by some $\boldsymbol{\theta}_k$, defines the computation, i.e. signal transmission, at layer \mathbf{L}_k where $\mathcal{I}_k := \{i_1(k), \dots, i_j(k)\} \subseteq \{0, 1, \dots, K-1\}$ are the indices of layers that feed into \mathbf{L}_k . That is, given an input signal $\bar{\mathbf{y}} \in \mathbb{R}^{d_0}$ assigned to \mathbf{L}_0 , a DNN is a composition of parameterized functions where

$$\mathbf{L}_k \equiv \mathbf{f}_k(\mathbf{L}_{i_1(k)}, \dots, \mathbf{L}_{i_j(k)}; \boldsymbol{\theta}_k) \in \mathbb{R}^{d_k}.$$

Standard convolutional neural networks, as an example, use $\mathcal{I}_k = \{k-1\}$ and $\mathbf{f}_k(\mathbf{L}_{k-1}; \boldsymbol{\theta}_k) = [\mathbf{W}_k, \mathbf{b}_k] = \sigma(\mathbf{W}_k \star \mathbf{L}_{k-1} + \mathbf{b}_k)$ where \mathbf{b}_k is an added bias, σ is an activation function applied componentwise, and $\mathbf{W}_k \star \mathbf{L}_{k-1}$ denotes the convolution of the weight kernel \mathbf{W}_k and input signal \mathbf{L}_{k-1} .

A DNN learns its parameters, $\boldsymbol{\Theta} = (\boldsymbol{\theta}_1, \dots, \boldsymbol{\theta}_K)$, by optimizing a loss function, $\mathcal{L}(\boldsymbol{\Theta})$, over a training dataset $\mathcal{D} = \{(\bar{\mathbf{y}}_i, \bar{\mathbf{c}}_i) : i = 1, 2, \dots, N_s\}$ where each $(\bar{\mathbf{y}}_i, \bar{\mathbf{c}}_i)$ satisfies equation (1). Let $\hat{\mathbf{c}}(\bar{\mathbf{y}}_i; \boldsymbol{\Theta})$ denote the DNN output given the input $\bar{\mathbf{y}}_i$ and parameterization $\boldsymbol{\Theta}$. Then the loss function is often defined as the average $\mathcal{L}(\boldsymbol{\Theta}) := \frac{1}{N_s} \sum_{i=1}^{N_s} L(\hat{\mathbf{c}}(\bar{\mathbf{y}}_i; \boldsymbol{\Theta}), \bar{\mathbf{c}}_i)$ where $L(\hat{\mathbf{c}}(\bar{\mathbf{y}}_i; \boldsymbol{\Theta}), \bar{\mathbf{c}}_i)$ is the loss, or error, between the network output, $\hat{\mathbf{c}}(\bar{\mathbf{y}}_i; \boldsymbol{\Theta})$, and the actual coefficients, $\bar{\mathbf{c}}_i$. Common loss functions for image reconstruction neural networks include mean-squared error (MSE), mean-absolute error (MAE), peak signal-to-noise ratio (PSNR), or structural similarity index measure (SSIM) [34]. After training the DNN, the

cascade of function compositions collectively models a desired transformation from an input space to an output space.

Algorithm unrolling creates a DNN by assigning the operations from each step, k , of any iterative algorithm as the function, f_k , defining layer k . That is, layer k in the DNN corresponds to the output of k iterations of the original iterative algorithm. Then parameters, θ_k , on each step, k , of the iterative algorithm parameterize f_k in the DNN [17, 18]. In training the unrolled DNN, each θ_k is learned, which optimizes the iterative algorithm.

III. ITERATIVE ALGORITHM: G-CG-LS

In order to solve the linear inverse problem to (1) for the unknown vector \mathbf{c} , we incorporate the CG prior into \mathbf{c} via (2) and perform the following optimization w.r.t. both the Gaussian, i.e. \mathbf{u} , and non-Gaussian, i.e. \mathbf{z} , components

$$[\mathbf{u}^* \quad \mathbf{z}^*] = \arg \min_{(\mathbf{u}, \mathbf{z}) \in \mathbb{R}^n \times \mathfrak{Z}} F(\mathbf{u}, \mathbf{z}) \quad (3)$$

where

$$F(\mathbf{u}, \mathbf{z}) := \frac{1}{2} \|\mathbf{y} - A(\mathbf{z} \odot \mathbf{u})\|_2^2 + \frac{1}{2} \mathbf{u}^T P_u^{-1} \mathbf{u} + \mathcal{R}(\mathbf{z}) \quad (4)$$

such that $\frac{1}{2} \|\mathbf{y} - A(\mathbf{z} \odot \mathbf{u})\|_2^2$ is defined as the data fidelity term, $P_u \propto \Sigma_u$, $\mathcal{R}(\mathbf{z}) \propto \log(p_{\mathbf{z}}(\mathbf{z}))$, and $\mathfrak{Z} \subseteq [0, \infty)^n$ is the domain of \mathcal{R} , which we assume to be convex. Our solution for the linear inverse problem to (1) is then given as $\mathbf{c}^* = \mathbf{u}^* \odot \mathbf{z}^*$.

Note that for additive white noise in (1), the estimate in (3) is equivalent to a MAP estimate (see Proposition 5 in the Appendix). Our G-CG-LS algorithm, given in Algorithm 1, is an iterative method to approximately solve (3) through block coordinate descent [35].

To detail Algorithm 1, define $A_{\mathbf{z}} = A \text{Diag}(\mathbf{z})$ and note that the minimization of (4) w.r.t. \mathbf{u} is a Tikhonov regularization, or ridge regression, problem with minimizer $\mathcal{T}(\mathbf{z}) \equiv \mathcal{T}(\mathbf{z}; P_u)$ defined as

$$\mathcal{T}(\mathbf{z}) := \arg \min_{\mathbf{u}} F(\mathbf{u}, \mathbf{z}) = (A_{\mathbf{z}}^T A_{\mathbf{z}} + P_u^{-1})^{-1} A_{\mathbf{z}}^T \mathbf{y}. \quad (5)$$

which we call the Tikhonov solution. For minimizing (4) w.r.t. \mathbf{z} , a number, J , of descent steps are iteratively applied. Let $g(\mathbf{z}, \mathbf{u}) : \mathbb{R}^n \times \mathbb{R}^n \rightarrow \mathbb{R}^n$ be a descent function of (4) w.r.t. \mathbf{z} ; we consider two possibilities for g as discussed in Section III-A. Then, the G-CG-LS estimate of \mathbf{z} on descent step j of iteration k and the G-CG-LS estimate of \mathbf{u} on iteration k are given respectively by

$$\mathbf{z}_k^{(j)} = g(\mathbf{z}_k^{(j-1)}, \mathbf{u}_{k-1}) \quad \text{and} \quad \mathbf{u}_k = \mathcal{T}(\mathbf{z}_k; P_u).$$

Note that we define $\mathbf{z}_k^{(J)} = \mathbf{z}_{k+1}^{(0)} \equiv \mathbf{z}_k$. Lastly, Algorithm 1 is initialized as $\mathbf{z}_0 = \mathcal{P}_{[0, b]^n}(A^T \mathbf{y})$ and $\mathbf{u}_0 = \mathcal{T}(\mathbf{z}_0)$. Using the rectified linear unit (ReLU) activation function, we remark that $\mathcal{P}_{[0, b]^n}(\mathbf{x}) = [\text{ReLU}(x_i) - \text{ReLU}(x_i - b)]_{i=1}^n$ and is applied to eliminate negative values in \mathbf{z}_0 and limit the maximum value in \mathbf{z}_0 for numerical stability in calculating \mathbf{u}_0 .

Note that the computational time to calculate (5) can be reduced by using the Woodbury matrix identity to express \mathcal{T} as (see Section II-B in the supplementary material)

$$\mathcal{T}(\mathbf{z}; P_u) = P_u A_{\mathbf{z}}^T (I + A_{\mathbf{z}} P_u A_{\mathbf{z}}^T)^{-1} \mathbf{y}, \quad (6)$$

Algorithm 1 G-CG-LS

```

1:  $\mathbf{z}_0 = \mathcal{P}_{[0, b]^n}(A^T \mathbf{y})$  and  $\mathbf{u}_0 = \mathcal{T}(\mathbf{z}_0)$  (or  $\tilde{\mathcal{T}}(\mathbf{0}, \mathbf{z}_0)$  for NAGD)
2: for  $k \in \{1, 2, \dots, K\}$  do
3:    $\mathbf{z}$  ESTIMATION:
4:    $\mathbf{z}_k^{(0)} = \mathbf{z}_{k-1}$ 
5:   for  $j \in \{1, 2, \dots, J\}$  do
6:      $\mathbf{z}_k^{(j)} = g(\mathbf{z}_k^{(j-1)}, \mathbf{u}_{k-1})$ 
7:   end for
8:    $\mathbf{z}_k = \mathbf{z}_k^{(J)}$ 
9:    $\mathbf{u}$  ESTIMATION:
10:   $\mathbf{u}_k = \mathcal{T}(\mathbf{z}_k)$  (or  $\tilde{\mathcal{T}}(\mathbf{u}_{k-1}, \mathbf{z}_k)$  for NAGD)
11: end for
Output:  $\mathbf{c}^* = \mathbf{z}_K \odot \mathbf{u}_K$ 

```

which turns the $n \times n$ linear system of equations in (5) into an $m \times m$ linear system of equations. Additionally, we remark that (4) is strongly convex w.r.t. \mathbf{u} and thus the Tikhonov solution is efficiently approximated by Nesterov accelerated gradient descent (NAGD) [36]. Hence, for sufficiently high-dimensional signals of interest, such that the linear solve in (6) is infeasible, we replace the exact calculation of (6) by a NAGD approximation. To detail the NAGD approximation, define for $\eta > 0$

$$\begin{aligned} r_u(\mathbf{u}, \mathbf{z}) &:= \mathbf{u} - \eta \nabla_{\mathbf{u}} F(\mathbf{u}, \mathbf{z}) \\ &= \mathbf{u} - \eta (A_{\mathbf{z}}^T (A_{\mathbf{z}} \mathbf{u} - \mathbf{y}) + P_u^{-1} \mathbf{u}). \end{aligned} \quad (7)$$

The estimate of \mathbf{u} on descent step $j+1$ of iteration k is then given by

$$\mathbf{u}_k^{(j+1)} = r_u(\mathbf{u}_k^{(j)}, \mathbf{z}_k) + \beta(r_u(\mathbf{u}_k^{(j)}, \mathbf{z}_k) - r_u(\mathbf{u}_k^{(j-1)}, \mathbf{z}_k))$$

where $\beta \geq 0$ is a momentum control parameter and $\mathbf{u}_k^{(0)} = \mathbf{u}_k^{(-1)} = \mathbf{u}_{k-1}$. Let J_u denote the number of NAGD steps, then the estimate of \mathbf{u} on iteration k is given as $\mathbf{u}_k = \mathbf{u}_k^{(J_u)}$. Note that we denote this composition of all J_u NAGD steps as $\tilde{\mathcal{T}}(\mathbf{u}, \mathbf{z}) \equiv \tilde{\mathcal{T}}(\mathbf{u}, \mathbf{z}; P_u)$ to emphasize that the NAGD estimate approximates the Tikhonov solution, \mathcal{T} . That is, $\mathbf{u}_k = \mathbf{u}_{k-1}^{(J_u)} = \tilde{\mathcal{T}}(\mathbf{u}_{k-1}, \mathbf{z}_k)$.

As our G-CG-LS method generalizes previous CG-based iterative algorithms [8, 26, 27], we briefly explain key differences. Previous works [8, 26, 27] similarly decompose \mathbf{c} via (2), but restrict $\mathbf{z} = h(\mathbf{x})$ where $\mathbf{x} \sim \mathcal{N}(\mathbf{0}, I)$ and h is an invertible nonlinear function. For this choice of \mathbf{z} , \mathcal{R} in (4) is set at $\mathcal{R}(\mathbf{z}) = \mu \|\mathbf{h}^{-1}(\mathbf{z})\|_2^2$, for scalar $\mu > 0$, to enforce normality of \mathbf{x} . Furthermore, previous work [8, 26, 27] restricts P_u in (4) to be a scaled identity matrix. Our G-CG-LS algorithm naturally generalizes these prior CG-based iterative algorithm cost functions to a cost function with implicit scale regularization, \mathcal{R} , and general covariance matrix structure. By applying algorithm unrolling to G-CG-LS, as shown in Section IV, \mathcal{R} and P_u can be optimally learned to produce a DNN with greater representational capacity and applicability than the unrolled CG-based DNNs proposed in [8, 26, 27].

A. Scale Variable Update Methods

Two methods we employ to minimize (4) w.r.t. \mathbf{z} are detailed below where $\eta > 0$ is a real-valued step size. Note that, for both methods, we define $A_{\mathbf{u}} = A \text{Diag}(\mathbf{u})$.

a) *Projected Gradient Descent (PGD)*:

$$\begin{aligned} g(\mathbf{z}, \mathbf{u}) &:= \mathcal{P}_3(\mathbf{z} - \eta \nabla_{\mathbf{z}} F(\mathbf{u}, \mathbf{z})) \\ &= \mathcal{P}_3(\mathbf{z} - \eta (A_{\mathbf{u}}^T (A_{\mathbf{u}} \mathbf{z} - \mathbf{y}) + \nabla \mathcal{R}(\mathbf{z}))) \end{aligned}$$

where \mathcal{P}_3 is the projection onto \mathcal{S} .

b) *Iterative Shrinkage and Thresholding (ISTA)*:

$$\begin{aligned} g(\mathbf{z}, \mathbf{u}) &:= \text{prox}_{\eta \mathcal{R}}(\mathbf{z} - \eta A_{\mathbf{u}}^T (A_{\mathbf{u}} \mathbf{z} - \mathbf{y})) \\ &= \arg \min_{\zeta \in \mathcal{S}} \frac{1}{2} \|\zeta - (\mathbf{z} - \eta A_{\mathbf{u}}^T (A_{\mathbf{u}} \mathbf{z} - \mathbf{y}))\|_2^2 + \eta \mathcal{R}(\zeta) \end{aligned}$$

where prox_f is the proximal operator of f and is well-defined for convex f . We remark that for a non-smooth, convex function, f , the proximal operator is an optimization tool as fixed points of prox_f minimize f . The general ISTA method, above in (b), which is equivalent to proximal gradient descent, is an optimization method for the sum of a convex, differentiable function and a convex, non-smooth function [2]. Using the proximal operator on the non-smooth function, fixed points of ISTA are optimality points of the original function sum (see Appendix VII-B).

The PGD and ISTA methods were chosen for their simplicity of implementation, provable convergence properties, and the success of unrolling ISTA for linear inverse problems [17, 19]–[21]. Additional details about PGD and ISTA, including backtracking linesearch methods and descent bounds, are given in Appendices VII-A and VII-B, respectively.

B. Convergence of G-CG-LS

This subsection provides theoretical convergence properties of G-CG-LS and can be skipped by those focused on implementation details. Convergence is proven in the Appendix under certain combinations of the following assumptions:

- (A1) \mathcal{R} is bounded below and satisfies $\lim_{z_i \rightarrow \infty} \mathcal{R}(\mathbf{z}) \rightarrow \infty$ for all $i = 1, 2, \dots, n$.
- (A2) \mathcal{R} is convex but possibly non-smooth.
- (A3) \mathcal{R} is twice continuously differentiable (i.e. $\mathcal{R} \in C^2$).

We first remark that (4) is strongly convex w.r.t. \mathbf{u} , with strength controlled by the spectral radius of $P_{\mathbf{u}}$ [28], and thus (4) has no maxima.

Proposition 1. *Let \mathcal{R} satisfy (A1). If \mathcal{R} satisfies (A2) for ISTA G-CG-LS or (A3) for PGD G-CG-LS, then the sequence $\{F(\mathbf{u}_k, \mathbf{z}_k)\}_{k=1}^{\infty}$ converges.*

Using Proposition 1, G-CG-LS converges to stationary points of (4) defined in Definition 1 of the Appendix.

Theorem 2. *Let \mathcal{R} satisfy (A1). If \mathcal{R} satisfies (A2) for ISTA G-CG-LS or (A3) for PGD G-CG-LS, then every limit point of the sequence $\{(\mathbf{u}_k, \mathbf{z}_k)\}_{k=1}^{\infty}$ is a stationary point of (4).*

Proof of Proposition 1 and Theorem 2 are in Appendix VII-C and Appendix VII-D, respectively. The proof of

Theorem 2 is inspired by ideas from [2, 37, 38], which consider the convergence of PGD and ISTA-type updates. Where [2, 37] consider a single block update, which we can transfer to individual updates of \mathbf{z} when \mathbf{u} is fixed, we distinctly have two block updates defining each iteration. While [38] considers multiblock updates, each block is updated by a single step of an identical method. Instead, we consider multiple steps and unique methods defining each block update.

Next, we discuss the convergence of the G-CG-LS estimates. For this, we say a sequence converges to set \mathcal{S} if the sequence values become arbitrarily close to elements of \mathcal{S} .

Proposition 3. *Let the assumptions of Theorem 2 hold. Then the sequence $\{(\mathbf{u}_k, \mathbf{z}_k)\}_{k=1}^{\infty}$ generated by ISTA G-CG-LS or PGD G-CG-LS converges to a closed connected set of stationary points of constant cost function value.*

Corollary 4. *Let the assumptions of Theorem 2 hold. Additionally, if \mathcal{R} is chosen such that (4) has nondegenerate stationary points then the ISTA G-CG-LS and PGD G-CG-LS sequences $\{(\mathbf{u}_k, \mathbf{z}_k)\}_{k=1}^{\infty}$ converge.*

Proofs of Proposition 3 and Corollary 4 are found in Appendix VII-E. We remark in choosing $\mathcal{R}(\mathbf{z})$ to be positively defined on an open domain, e.g. $\mathcal{R}(\mathbf{z}) = \|\log(\mathbf{z})\|_2^2$ defined on $(0, \infty)^n$, all stationary points are internal points and, consequently, the assumptions of Theorem 2 and Corollary 4 hold, implying G-CG-LS converges to a limit point of zero gradient (or zero subdifferential when \mathcal{R} is convex). In choosing $\mathcal{R}(\mathbf{z}) \propto -\log(p_{\mathbf{z}}(\mathbf{z}))$, as in a MAP estimate, many prior distributions, $p_{\mathbf{z}}$, produce $\mathcal{R}(\mathbf{z})$ defined only on the open domain $(0, \infty)^n$. Specifically, any twice continuously differentiable distribution satisfying $\lim_{z_i \rightarrow 0} p_{\mathbf{z}}(\mathbf{z}) \rightarrow 0$ will produce \mathcal{R} only defined on $(0, \infty)^n$, thus satisfying the PGD assumptions of Theorem 2. Examples of such \mathbf{z} distributions useful in modeling image coefficients include log-normal and Gamma($\alpha, 1$) for $\alpha > 1$ distributions [6, 7, 29].

IV. DR-CG-NET

A. Network Structure

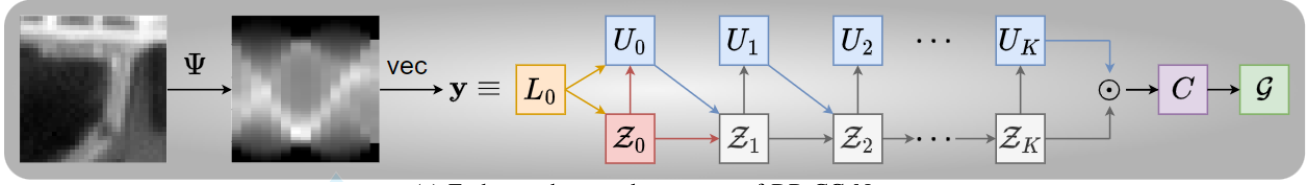
We create a DNN named DR-CG-Net, with the end-to-end structure shown in Fig. 1a, by applying algorithm unrolling to G-CG-LS in Algorithm 1. Instead of requiring a specified \mathcal{R} , DR-CG-Net learns \mathcal{R} through a subnetwork representing either $\nabla \mathcal{R}$ or $\text{prox}_{\eta \mathcal{R}}$.

Let $\mathcal{V}_k^{(j)} : \mathbb{R}^n \rightarrow \mathbb{R}^n$, for $k = 1, 2, \dots, K$ and $j = 1, 2, \dots, J$, be a subnetwork. That is, each $\mathcal{V}_k^{(j)}$ is a collection of layers mapping from \mathbb{R}^n to \mathbb{R}^n . The particular form of $\mathcal{V}_k^{(j)}$ we employ is given in Section IV-B. Following the scale variable updates of Section III-A we define the intermediate scale variable mapping, $g_k^{(j)}$, as

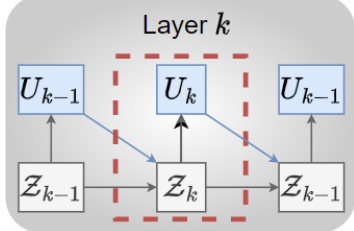
$$g_k^{(j)}(\mathbf{z}, \mathbf{u}) := \begin{cases} \text{ReLU}\left(r_k^{(j)}(\mathbf{z}, \mathbf{u}) + \mathcal{V}_k^{(j)}(\mathbf{z})\right) & \text{PGD} \\ \text{ReLU}\left(\mathcal{V}_k^{(j)}\left(r_k^{(j)}(\mathbf{z}, \mathbf{u})\right)\right) & \text{ISTA} \end{cases} \quad (8)$$

where $r_k^{(j)}$ is a data fidelity gradient descent step of (4) in \mathbf{z} ,

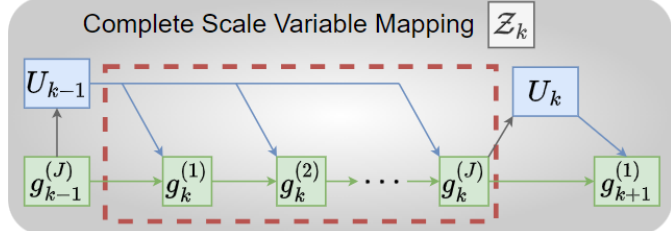
$$r_k^{(j)}(\mathbf{z}, \mathbf{u}) = \mathbf{z} - \eta_k^{(j)} A_{\mathbf{u}}^T (A_{\mathbf{u}} \mathbf{z} - \mathbf{y}) \quad (9)$$



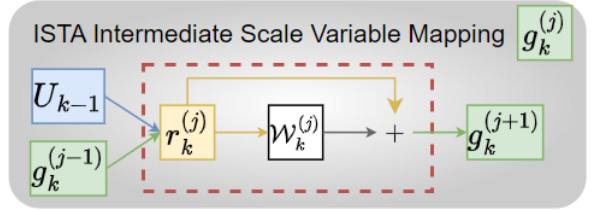
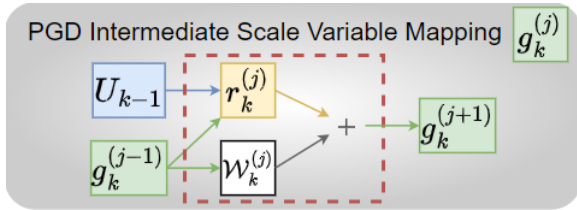
(a) End-to-end network structure of DR-CG-Net.



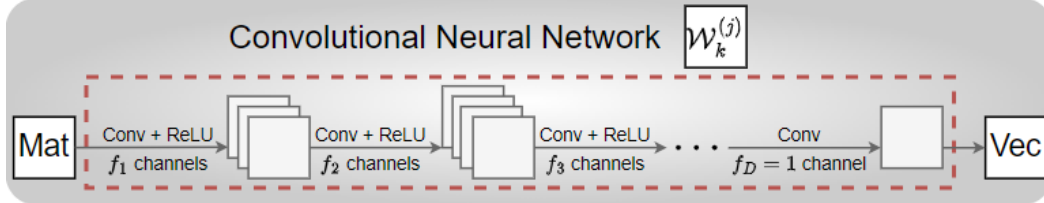
(b) Layer k analogous to iteration k of Algorithm 1.



(c) Complete scale variable mapping, Z_k , producing estimate z_k in Algorithm 1.



(d) Intermediate scale variable mapping, $g_k^{(j)}$, for PGD (left) and ISTA (right) which produces the estimate, $z_k^{(j)}$, in Algorithm 1.



(e) Network representing $\nabla \mathcal{R}$ or $\text{prox}_{\eta \mathcal{R}}$ for PGD or ISTA, respectively. No bias is added, ReLU activation functions are employed, and f_1, f_2, \dots , and f_D denote the integer number of output filter channels. Mat converts a vector into a matrix and Vec inverts this process.

Fig. 1: End-to-end network structure for DR-CG-Net, the unrolled deep neural network of Algorithm 1, is shown in (1a). DR-CG-Net consists of an input block, L_0 , initialization block, Z_0 , $K + 1$ Tikhonov blocks, U_k , K complete scale variable mappings, Z_k , a Hadamard product block, C , and an optional refinement block, G . Each Z_k , with structure in (1c), consists of J updates $g_k^{(j)}$ further detailed in (1d). Each $g_k^{(j)}$ consists of a data fidelity gradient descent step, $r_k^{(j)}$, added to a convolutional neural network, $W_k^{(j)}$ in (1e), and corresponds to an intermediate update of the z variable.

for a step size $\eta_k^{(j)}$. Note that we apply the ReLU function componentwise in (8), where $\text{ReLU} \equiv \mathcal{P}_{[0, \infty)}$, to ensure all z estimates in DR-CG-Net maintain positive entries.

Each layer k of DR-CG-Net, shown in Fig. 1b, is broken down into a complete scale variable mapping block, Z_k shown in Fig. 1c, and a Tikhonov solution block, U_k , so that layer k corresponds to iteration k of Algorithm 1. As in Algorithm 1, Z_k consists of a composition of the J scale variable update blocks $g_k^{(1)}, \dots, g_k^{(J)}$ shown in Fig. 1d for PGD or ISTA.

Mathematically detailing the DR-CG-Net blocks we have:

$L_0 = \mathbf{y}$ is the input measurements to the network.

$Z_0 = \mathcal{P}_{[0, b]^n}(\hat{A}^T \mathbf{y})$, for $\hat{A} = A/\|A\|_2$, is the initial estimate of z from line 1 of Algorithm 1.

$U_k = \mathcal{T}(g_k^{(J)}; P_k)$ (or $\tilde{\mathcal{T}}(U_{k-1}, g_k^{(J)}; P_k)$ for NAGD), for covariance matrix P_k , is the Tikhonov estimate corresponding to line 1 and 10 of Algorithm 1.

The k th complete scale variable mapping Z_k contains:

$g_k^{(j)} = g_k^{(j)}(g_k^{(j-1)}, U_{k-1})$ is an intermediate scale variable mapping analogous to $z_k^{(j)}$ on line 6 in Algorithm 1.

$r_k^{(j)} = r_k^{(j)}(g_k^{(j-1)}, U_{k-1})$ is the data fidelity gradient step.

$W_k^{(j)} = D$ layer convolutional neural network.

$C = U_K \odot Z_K$ is an estimate of the signal, c .

$G = g_{K+1}^{(1)}(C, \mathbf{1})$ is an optional refinement of the estimated signal, c , producing the DR-CG-Net output.

Note, to simplify notation, we let $g_k^{(0)} = g_{k-1}^{(J)}$, $U_{-1} = \mathbf{0}$, and $\mathbf{1} \in \mathbb{R}^n$ be a vector of ones. We remark that the optional refinement block G deviates from the structure of G-CG-LS and instead corresponds to an unrolled PGD or ISTA step on the cost function $\tilde{F}(c) := \frac{1}{2} \|\mathbf{y} - Ac\|_2^2 + \tilde{\mathcal{R}}(c)$ where $\tilde{\mathcal{R}}(c)$ is a learned implicit regularization on the total signal, c . As (4) is a special case of \tilde{F} , where the CG decomposition from (2) is used to split c , the refinement block simultaneously updates

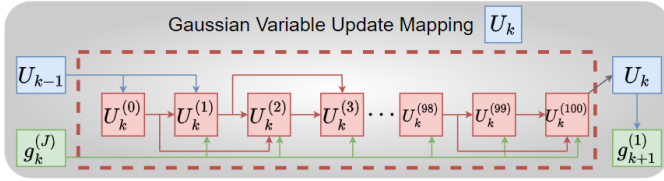


Fig. 2: Structure of the u update block, U_k , for using gradient descent steps with Nesterov momentum.

both z and u such that the interrelationship between these fields is best exploited for the signal of interest.

The refinement block is motivated, in part, by prior art approaches, such as MADUN [19] and ISTA-Net⁺ [20], that model each DNN layer as an ISTA-type step on the cost function \tilde{F} . As such, our DR-CG-Net approach first exploits the powerful CG prior through minimizing (4) to obtain a high quality estimate for the inverse problem to (1), and subsequently fine-tunes this estimate through the optional refinement block that mimics a single layer of these prior art methods. Empirically shown in Section V-E, the unrolled G-CG-LS portion of DR-CG-Net, that is up to and including block C , is the core component in signal reconstruction performance and that the refinement block marginally refines, e.g. denoises, the final estimate C .

Finally, as discussed in Section III, for significantly high-dimensional signals of interest, the U_k block contains J_u NAGD steps as detailed in Fig. 2. Using (7), we define the intermediate Gaussian variable mapping, $g_u(u, w, z; \beta)$, as

$$g_u(u, w, z; \beta) := r_u(u, z) + \beta (r_u(u, z) - r_u(w, z)).$$

Then, $U_k^{(j)}$ in Fig. 2 is given by

$$U_k^{(j)} = g_u \left(U_k^{(j-1)}, U_k^{(j-2)}, g_k^{(j)}; 1 - \frac{3}{6+j} \right) \text{ is a NAGD step.}$$

Note that we set $U_k^{(0)} = U_k^{(-1)} \equiv U_{k-1}$ and choose an adaptive momentum parameter of $1 - \frac{3}{6+j}$, for j the NAGD step count, as proposed in [36]. For this setting, the U_k block is given by the approximation of the Tikhonov solution $\tilde{\mathcal{T}}$ rather the exact Tikhonov solution \mathcal{T} .

B. Network Parameters and Subnetwork

For every $k = 0, 1, \dots, K$, the layer U_k is parameterized by a covariance matrix, P_k . To reduce the number of parameters learned by the network and for consistency in P_k representing the covariance matrix of u , DR-CG-Net learns a single covariance matrix P and constrains $P_1 = \dots = P_K = P$. Furthermore, we consider the possibility of a structured covariance matrix where P is either a scaled identity, diagonal, tridiagonal, or full matrix. Imposing a covariance structure may be desirable or advantageous, for example, to ensure only local reinforcement.

We remark that to ensure P is a covariance matrix, i.e. symmetric and positive definite, we impose, for $\epsilon > 0$ a small

fixed real number, one of the following structures

$$P = \begin{cases} \max\{\lambda, \epsilon\}I & \text{Scaled Identity} \\ \text{Diag}([\max\{\lambda_i, \epsilon\}]_{i=1}^n) & \text{Diagonal} \\ L_{\text{tri}}L_{\text{tri}}^T + \epsilon I & \text{Tridiagonal} \\ LL^T + \epsilon I & \text{Full.} \end{cases}$$

In the scaled identity case, only a constant λ is learned. In the diagonal case, a vector $\lambda = [\lambda_i]_{i=1}^n$ is learned. In the tridiagonal case, two vectors $\lambda_1 \in \mathbb{R}^n$ and $\lambda_2 \in \mathbb{R}^{n-1}$ are learned such that the lower triangular matrix component L_{tri} is formed by placing λ_1 on the diagonal and λ_2 on the first subdiagonal. Finally, in the case of a full covariance matrix, an entire lower triangular matrix, L , is learned.

Next, each \mathcal{Z}_k is parameterized both by a collection of step sizes $\{\eta_k^{(1)}, \dots, \eta_k^{(J)}\}$ (as $\eta_k^{(j)}$ parameterizes the data fidelity gradient step, $r_k^{(j)}$) and by the parameters of the subnetworks $\mathcal{V}_k^{(1)}, \dots, \mathcal{V}_k^{(J)}$. Similarly, the refinement block is parameterized by a step size $\eta_{K+1}^{(1)}$ and subnetwork $\mathcal{V}_{K+1}^{(1)}$.

For the step sizes, we take $\eta_k^{(j)}$ from (9) as

$$\eta_k^{(j)} = \delta_k^{(j)} \begin{cases} 1 & \|A_u^T(A_u z - y)\|_2 \leq \gamma_{\max} \\ \frac{\gamma_{\max}}{\|A_u^T(A_u z - y)\|_2} & \text{else} \end{cases}$$

for fixed constant $\gamma_{\max} > 0$ and a learned real-valued parameter $\delta_k^{(j)}$. This is a slight variation on normalized gradient descent [39] for the data fidelity term of (4), which we empirically find to provide stability. In particular, normalized gradient descent supplies sample-specific step size adjustments to prevent a large and counterproductive gradient descent step.

For the subnetworks, let $\mathcal{W}_k^{(j)}$ be a CNN of depth D using ReLU activation functions where the convolutions in layer d use $k_d \times k_d$ kernel size and produce f_d output filter channels as shown in Fig. 1e. Note, zero padding is applied to each filter channel of the input such that the output at each filter channel is the same size as the input. Furthermore, we take $f_D = 1$ such that for $X \in \mathbb{R}^{n \times n}$ we have $\mathcal{W}_k^{(j)}(X) \in \mathbb{R}^{n \times n}$. Next, for $x \in \mathbb{R}^{n^2}$ we define $\text{mat}(x)$ to be x reshaped into a $n \times n$ matrix. Similarly, for $X \in \mathbb{R}^{n \times n}$, we define $\text{vec}(X)$ to be X reshaped into a vector of size n^2 such that $\text{vec}(\text{mat}(x)) = x$. Then we set

$$\mathcal{V}_k^{(j)}(x) = \begin{cases} \text{vec}(\mathcal{W}_k^{(j)}(\text{mat}(x))) & \text{PGD} \\ x + \text{vec}(\mathcal{W}_k^{(j)}(\text{mat}(x))) & \text{ISTA.} \end{cases}$$

Define $\mathcal{W}_{k,d}^{(j)}$, for $d = 1, 2, \dots, D$, as the convolutional weight kernels of $\mathcal{W}_k^{(j)}$, which also parameterize the subnetwork $\mathcal{V}_k^{(j)}$.

From the above, the DR-CG-Net parameters are

$$\Theta = \{P\} \cup \left\{ \delta_k^{(j)}, \mathcal{W}_{k,d}^{(j)}, \delta_{K+1}^{(1)}, \mathcal{W}_{K+1,d}^{(1)} \right\}_{\substack{j=1,2,\dots,J \\ k=1,2,\dots,K \\ d=1,2,\dots,D}}.$$

Let $f_0 = 1$, $p = \sum_{d=1}^D f_{d-1} f_d k_d^2$, and $\dim(\mathcal{P}) = 1, n, 2n-1$, or $n(n+1)/2$ for the scaled identity, diagonal, tridiagonal, or full covariance matrix structures, respectively. Then DR-CG-Net has $\dim(\mathcal{P}) + (KJ+1)(p+1)$ total parameters.

C. Loss Function

The DR-CG-Net parameters are trained by minimizing the MAE loss function given as

$$\mathcal{L}_{\mathcal{B}}(\Theta) = \frac{1}{|\mathcal{B}|} \frac{1}{n} \sum_{(\bar{\mathbf{y}}_i, \bar{\mathbf{c}}_i) \in \mathcal{B}} \|\hat{\mathbf{c}}(\bar{\mathbf{y}}_i; \Theta) - \bar{\mathbf{c}}_i\|_1 \quad (10)$$

where \mathcal{B} is a batch of data points. The MAE loss function is optimized with adaptive moment estimation (Adam) [40], which is a stochastic, gradient-based optimizer. The gradient, $\nabla_{\Theta} \mathcal{L}_{\mathcal{B}}$, for Adam is calculated via backpropagation through the network, which we implement with automatic differentiation using TensorFlow [41].

V. NUMERICAL RESULTS

We consider two types of DR-CG-Nets, called PGD DR-CG-Net and ISTA DR-CG-Net, corresponding, respectively, to using the PGD or ISTA intermediate scale variable mapping given in (8). For unrolled iterations we set $(K, J) = (3, 4)$ for 32×32 images and $(K, J) = (1, 24)$ for all larger images. Each $\mathcal{V}_k^{(j)}$ is a CNN with depth $D = 8$. The network size was chosen empirically such that the time to complete a signal reconstruction was reasonably quick while still producing excellent reconstructions on a validation dataset. Every convolution uses a 3×3 kernel initialized according to the Glorot Uniform distribution [42] with ReLU activation functions and $f_1 = \dots = f_7 = 32$ and $f_8 = 1$ filter channels.

We initialize each step size as $\delta_k^{(j)} = 1$, set $\gamma_{\max} = 1$, and fix $\epsilon = 10^{-4}$. Each P_u structure is initialized as a diagonal matrix with 0.1 or 10 on the diagonal for Radon transform or Gaussian measurements, respectively. Additionally, for the initial \mathbf{z} estimate, we set $\mathcal{P}_{[0, b]^n} = \mathcal{P}_{[0, 10]^n}$. We train all DR-CG-Nets for 2000 epochs at a learning rate of 10^{-4} implementing early stopping to prevent overfitting.

We compare DR-CG-Net against ten state-of-the-art methods: (i) compound Gaussian network (CG-Net) [8, 26], (ii) memory augmented deep unfolding network (MADUN) [19], (iii) ISTA-Net⁺ [20], (iv) FISTA-Net [21], (v) iPiano-Net [24], (vi) ReconNet [11], (vii) LEARN⁺⁺ [23], (viii) Learned Primal-Dual (LPD) [25], (ix) FBPCovNet [12], and (x) iRadonMAP [13]. Although memory augmented proximal unrolled network (MAPUN) [43] was considered, due to the similarity in performance to MADUN only MADUN results are shown. Finally, two model-based approaches, filtered back-projection (FBP) [44] and super-voxel model-based iterative reconstruction (svMBIR) [45], are compared. As these model-based approaches are generally not as competitive as the top deep-learning methods, their results are relegated to the single plot of Fig. 7 to provide a baseline.

Note that LEARN⁺⁺, LPD, FBPCovNet, and iRadonMAP are CT-specific methods relying on the CT sinogram measurement structure. On the other hand, MADUN, ISTA-Net⁺, FISTA-Net, iPiano-Net, and ReconNet are reconstruction methods with particular application in image CS. Furthermore, we remark that CG-Net, MADUN, ISTA-Net⁺, FISTA-Net, iPiano-Net, LEARN⁺⁺, and LPD are DNNs formed by algorithm unrolling while ReconNet, iRadonMAP, and

FBPCovNet are instead standard DNNs. Lastly, as with DR-CG-Net, a refinement block is added to, and trained with, each CG-Net.

A. Data

We use 32×32 CIFAR10 images [46], 64×64 CalTech101 images [47], and 128×128 LoDoPaB-CT images [48]. Each image has been converted to a single-channel grayscale image, scaled down by the maximum pixel value, and vectorized. We apply a given sensing method, Ψ , to each image after which white noise is added producing noisy measurements, \mathbf{y} , at a specified SNR. This produces a dataset $\mathcal{D}_{N_s} = \{(\bar{\mathbf{y}}_i, \bar{\mathbf{c}}_i) : i = 1, 2, \dots, N_s\}$ where N_s is the number of data samples. Note that we randomly sample across all classes of images from CIFAR10 and CalTech101 in forming the training, validation, and testing datasets.

We consider two types of sensing matrices:

- 1) Radon Transform: Typical in tomography, specifically X-ray computed tomography, we form sensing matrices, Ψ , corresponding to Radon transforms at a number of uniformly spaced angles.
- 2) Random Gaussian Matrix: Typical in CS, $\Psi \in \mathbb{R}^{m \times n}$ has entries sampled from a standard Gaussian distribution with a given sampling ratio defined at $\frac{m}{n}$. We form three sensing matrices corresponding to sampling ratios of 0.5, 0.3, and 0.1.

Finally, we consider measurements with two different SNRs of 60dB or 40dB.

B. Main Results

For each set of data discussed in Section V-A, we train an ISTA DR-CG-Net, PGD DR-CG-Net, and each of the ten comparison methods, described at the beginning of this section, using varying amounts of training dataset sizes. For CIFAR10 images, the training datasets consist of $N_s = 20, 100, 500, 1000$, and 2000 data samples and, after training, 8000 test data samples are provided to every network to assess its performance. From varying the amount of training data, we find that a core utility of DR-CG-Net is its superior performance on small training datasets, i.e. a highly underdetermined system in (10). As such, for CalTech101 and LoDoPaB-CT images, we use training datasets with $N_s = 20$ samples, to focus on evaluating low training scenarios in greater detail, and 200 test data samples are provided to every network after training.

Average PSNR and SSIM quality metrics, together with associated 99% confidence intervals, on the test dataset reconstructions are used to evaluate network performance where higher values of these metrics correspond to reconstructed images that more closely match the original images. Note that the test data samples are formed from the same sensing matrix and noise level that produced the training data.

We remark that every method was trained using early stopping. That is, as shown in Fig. 12 in the supplementary material, training was conducted until the model initially overfits as compared to a validation dataset. In doing so, we

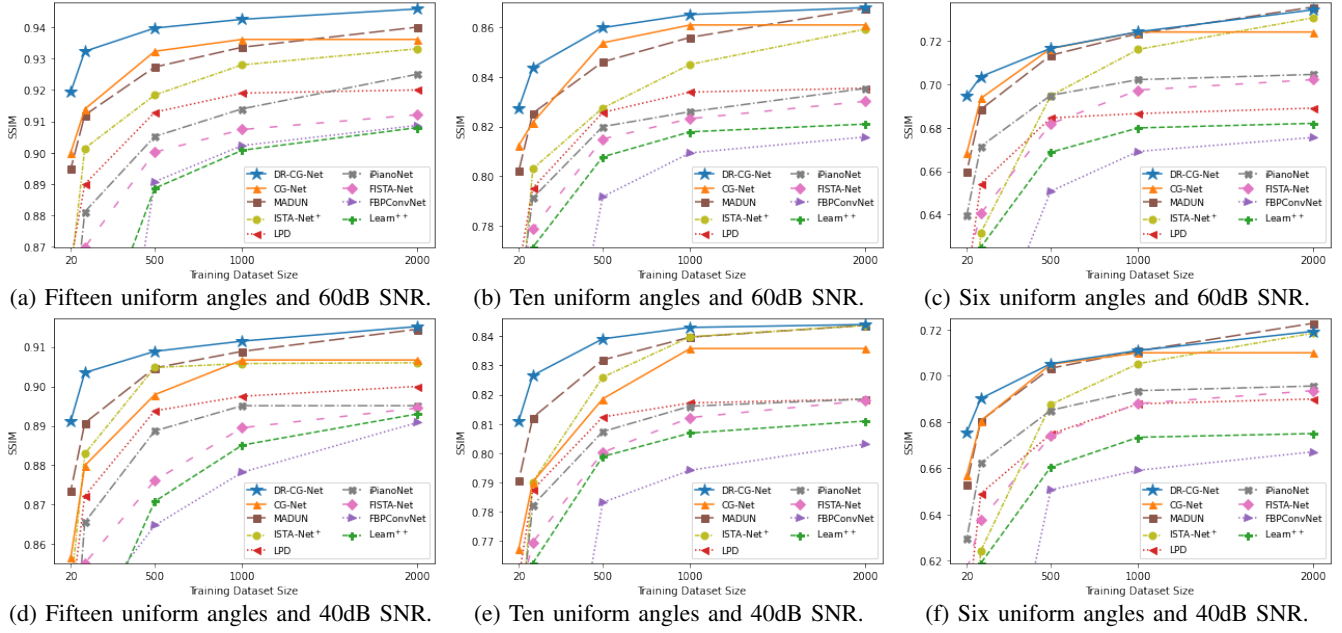


Fig. 3: Average test image reconstruction SSIM when varying the amount of CIFAR10 data in training nine machine learning-based image reconstruction methods. Here, the sensing matrices, Ψ , are a Radon transform at 15, 10, or 6 uniformly spaced angles, $\Phi = I$, and the measurement SNR is 60dB or 40dB. **Our DR-CG-Net method outperforms the compared prior art methods, in all scenarios, and does so appreciably in low training.**

ensure every model is sufficiently trained while also not being over-trained thereby presenting the best performance for each model for the provided set of training data.

For training datasets of size 20 and 100, we set P_u as a scaled identity covariance matrix and a tridiagonal covariance matrix is used for all other training datasets. Next, for images larger than 64×64 we approximate the Tikhonov solution with 100 NAGD steps as detailed in Fig. 2. Lastly, for Radon inversion experiments, we take $\Phi = I$ allowing DR-CG-Net to intrinsically learn the optimal signal representation basis.

Shown in Fig. 3 is the average SSIM quality over a set of test CIFAR10 image reconstructions from 60dB or 40dB SNR Radon transform measurements when varying the amount of training data. As ReconNet and iRadonMAP perform significantly lower they are omitted from Fig. 3. Additionally, as PGD DR-CG-Net performs equivalently to ISTA DR-CG-Net it too was omitted from Fig. 3. Note that Fig. 8 in the supplementary material displays similar plots for PSNR quality. We can see from Fig. 3, and Fig. 8 in the supplementary material, that DR-CG-Net outperforms, or performs comparably to, all compared methods in every training scenario and excels significantly in the lowest training scenarios of $N_s = 20$ and $N_s = 100$. However, the improvement of DR-CG-Net, over the comparison methods, diminishes when a greater amount of measurement noise is present and as the amount of training data increases. In particular, we observe from Fig. 3 that with enough training data and higher noise, DR-CG-Net can be matched by the best comparison method.

A visual comparison of all methods after training on only $N_s = 20$ samples is provided in Fig. 4, Fig. 6, and Fig. 7. In Fig. 4 are the estimates of a 128×128 scan from a Radon

transform at 60 uniformly spaced angles with 60dB SNR. Fig. 6 displays the reconstructions of a 64×64 test image from a Gaussian measurement at 0.5 sampling ratio. Lastly, Fig. 7 shows the estimates of a 64×64 test image from a Radon transform at 30 uniformly spaced angles. Additional visualizations, after training on $N_s = 20$ LoDoPaB-CT and CIFAR10 samples, are presented in Fig. 9 and Fig. 10 in the supplementary material. Fig. 9 and Fig. 10 display reconstructed images from a 76 angle Radon transform and from a Gaussian measurement with 0.5 sampling ratio, respectively. In each case, we see that ISTA and PGD DR-CG-Net perform comparably with both producing superior reconstructions, both visually and by SSIM, to all compared methods.

Fig. 5 further highlights the excellent performance of DR-CG-Net over the competitive methods in low training scenarios by providing the average SSIM over 200 test images, with 99% confidence intervals, after training only with $N_s = 20$ LoDoPaB-CT or CalTech101 images. In particular, Fig. 5a and Fig. 5b show the SSIM performance of all methods for reconstructing test images from Radon transform measurements. Fig. 5c shows the SSIM performance of all methods for reconstructing test images from Gaussian measurements. Observing Fig. 5, DR-CG-Net outperforms each prior art method, in both Radon inversion and CS tasks when training on limited datasets. We remark that PGD DR-CG-Net performs similarly to ISTA DR-CG-Net and is thus omitted from Fig. 5. As ReconNet and iRadonMAP perform the lowest, they are omitted from Fig. 5. Additionally, CG-Net is omitted from Fig. 5a due to an insurmountable computational cost to train on 128×128 images. Lastly, as LPD, LEARN⁺⁺, and FBPCConvNet are CT-specific methods, the CS problem is not

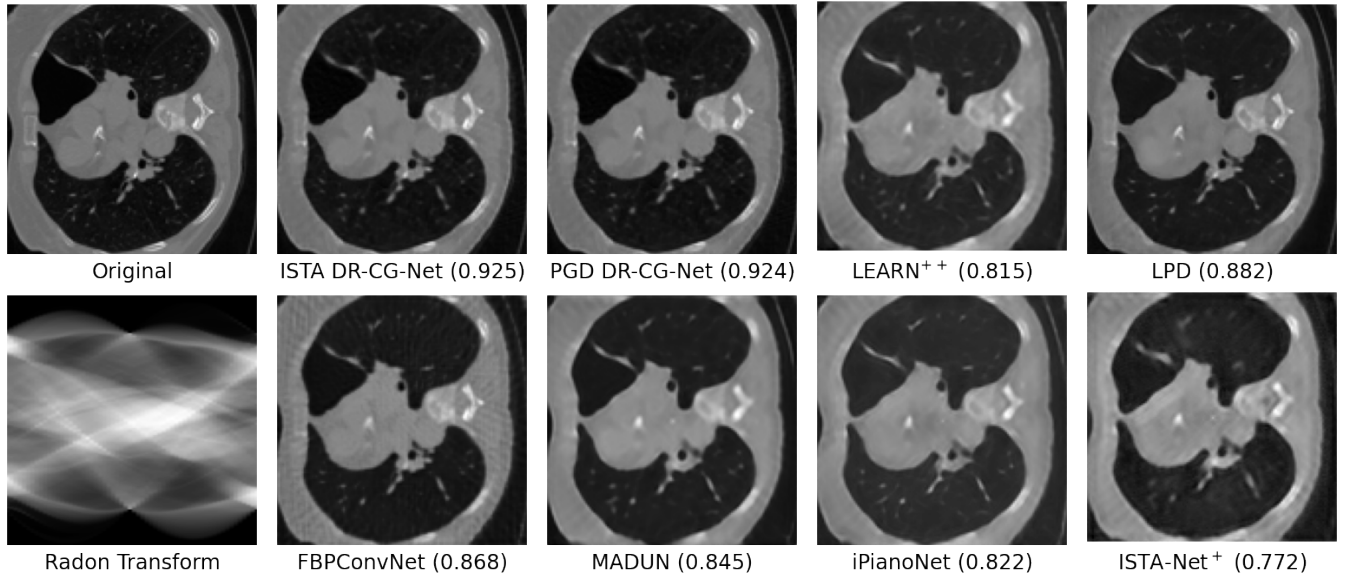


Fig. 4: Image reconstructions (SSIM) using our DR-CG-Net and six competitive deep learning methods on a 128×128 test scan after training with only 20 samples. The sensing matrix, Ψ , is a Radon transform at 60 uniformly spaced angles, $\Phi = I$, and each measurement has an SNR of 60dB. Our DR-CG-Net methods perform best visually and by SSIM.

applicable and so these comparisons are omitted from Fig. 5c.

An advantage of DR-CG-Net, as highlighted by our CIFAR10 and CalTech101 results in Fig. 3, Fig. 5, Fig. 6, and Fig. 7 is its ability to perform well on non-uniform data. Both CIFAR10 and CalTech101 contain many distinct classes of images from which we uniformly sample to create our training and testing datasets. In training with only 20 samples, few if any samples from each class will be seen by the network. Despite this, DR-CG-Net is able to recover high quality images in the test dataset that contains many more samples from both the classes present in the training data and from classes not present in the training data. That is, DR-CG-Net has the ability to learn only from a handful of samples in a class and generalize well to unseen classes of samples.

We posit that the high performance of DR-CG-Net, especially in low training scenarios, is due to the natural incorporation of the powerful CG prior through unrolling G-CGLS. Specifically, the Tikhonov estimation layers and Hadamard product layer provide significant data consistency structure by closely matching input measurements and measured estimated signals. Through this data consistency, a natural regularization for the DNN optimization is enforced by restricting the possible generated signals to a CG class. A thorough examination of the interplay between the iterative algorithm regularization and regularization for the DNN optimization is an intriguing subject of future work for unrolled DNN methods as a whole. Finally, the ability to learn the scale variable distribution, unlike in CG-Net where it is fixed as log-normal, provides DR-CG-Net with greater training capacity and flexibility to edge out CG-Net in test reconstruction performance in low training and significantly outperform CG-Net in higher training.

Lastly, we reiterate that the results of Fig. 4, 5, 6, 7, and in the supplementary material are for training on limited datasets, which is of interest in many applications in tomographic

imaging. Consequently, the results presented are not representative of the performance of these methods with unlimited training data where our method is likely to be matched by the comparison methods as indicated by the results in Fig. 3.

C. Computational Time and Complexity

Table I lists the average computational time per image, in milliseconds, across 8000 test image reconstructions running on a 64-bit Intel(R) Xeon(R) CPU E5-2690. Among the competing methods, we see that DR-CG-Net is comparable in reconstruction time to MADUN. While CG-Net provided the second-best results in low training scenarios, we can see from Table I that DR-CG-Net is, by comparison, at least 20 times faster on average in reconstructing images.

The speed increase of DR-CG-Net over CG-Net is from three main sources: First, each update of z in CG-Net implements an eigendecomposition calculation, which is slower than each z update in DR-CG-Net requiring only matrix-vector products. Second, CG-Net was formed by unrolling a larger number of iterations, specifically $(K, J) = (20, 1)$, whereas DR-CG-Net only requires $(K, J) = (3, 4)$ for excellent performance. Third, the Woodbury matrix identity is employed in DR-CG-Net to accelerate calculating the Tikhonov solution.

To explore the scalability of DR-CG-Net we consider the computational complexity of a forward pass through the

TABLE I: Average reconstruction time of 32×32 images from Radon transform measurements at 15 uniform angles.

Method	PGD DR-CG-Net	ISTA DR-CG-Net	CG-Net	MADUN
Time (ms)	22.0	52.7	765	26.0
Method	ReconNet	iRadonMAP	LEARN++	LPD
Time (ms)	0.65	4.5	10.6	4.7
Method	FBPCovNet	iPiano-Net	FISTA-Net	ISTA-Net+
Time (ms)	2.0	13.0	6.4	7.9

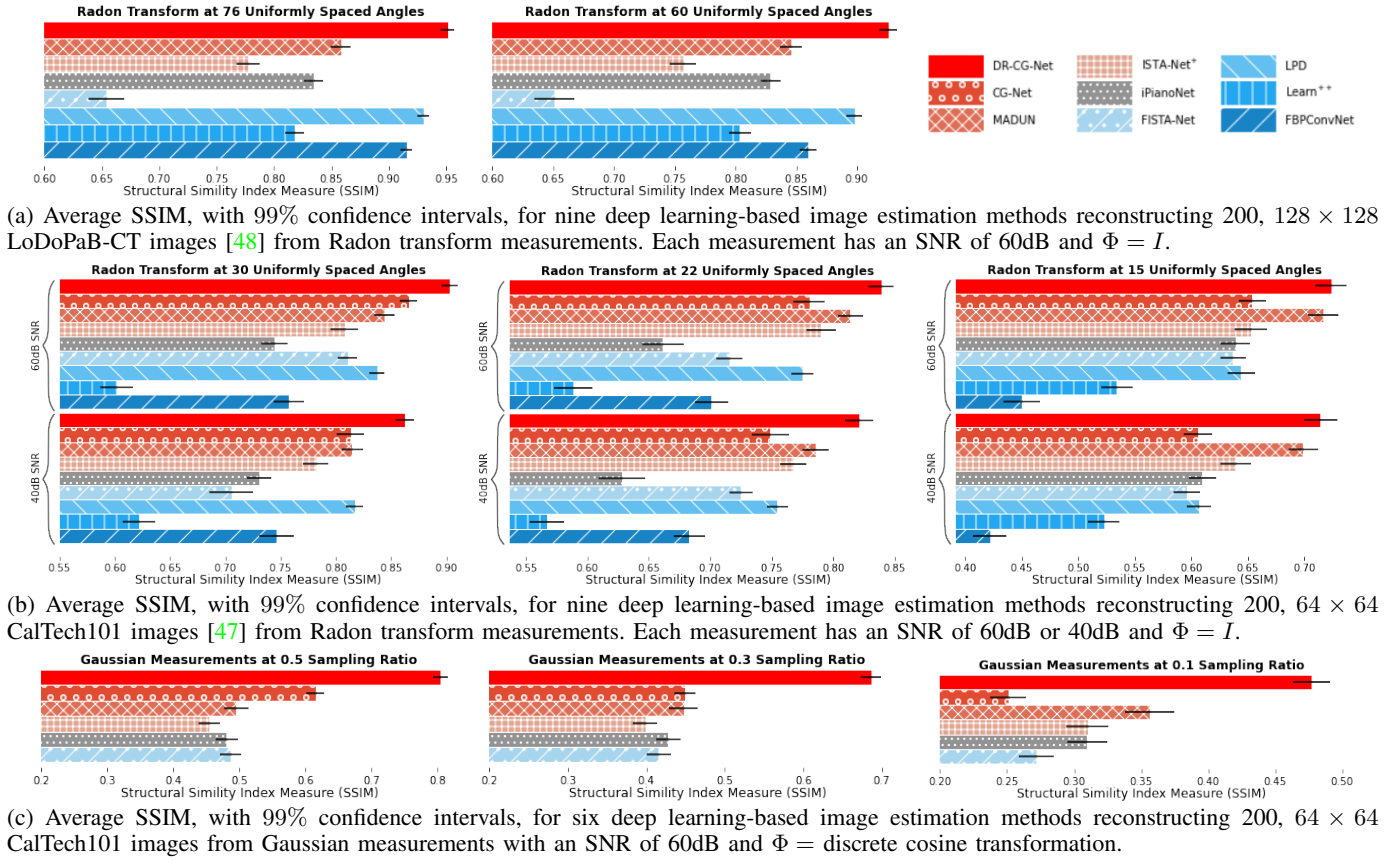


Fig. 5: Test image reconstruction quality for deep learning-based image estimation methods trained on only 20 samples. **In all cases, our method, DR-CG-Net given by the top solid red bar, outperforms the other approaches.**

network, in floating-point operations (FLOPs), with respect to the signal of interest size, n , and measurement size, m . We assume a batch size of one as the complexity simply grows proportionally to batch size. Block \mathcal{Z}_0 requires one matrix-vector product using $2mn$ FLOPs. For $i \geq 1$, block \mathcal{Z}_i requires one data fidelity gradient update, $r_k^{(j)}$, via (9) using $4mn + 4n + m$ FLOPs, D convolutions with 3×3 kernels and f_1, \dots, f_D filter channels using $18n \sum_{d=1}^D f_d$ FLOPs, and finally one addition of length n vectors using n FLOPs.

In the exact calculation of the Tikhonov solution via (6), first $I + A_z P_u A_z^T$ is calculated using $2mn^2 + 2m^2n + mn + m$ FLOPs. Second, a $m \times m$ system of equations is solved, naively using $\frac{2}{3}m^3 + \mathcal{O}(m^2)$ FLOPs. Finally, a $m \times n$ matrix vector product and $n \times n$ matrix vector product are performed using $2mn$ and $2n^2$ FLOPs, respectively. Thus, a total of $\frac{2}{3}m^3 + 2mn^2 + \mathcal{O}(m^2n + n^2)$ FLOPs are used in calculating (6). Therefore, when we calculate the Tikhonov solution exactly, the total FLOPs for DR-CG-Net scales as

$$\mathcal{O} \left(KJ \left[m + \sum_{d=1}^D f_d \right] n + Km^3 + Kmn^2 \right).$$

When we consider, instead, the approximation of the Tikhonov solution by J_u NAGD steps, the first two evaluations of r_u via (7) are computed, using $2n^2 + 4mn + 5n + m$ FLOPs each. Second, a length- n vector subtraction, scalar multiplication, and length- n vector addition are calculated using $3n$ FLOPs. Therefore, when we approximate the Tikhonov

solution with NAGD steps, the total FLOPs for DR-CG-Net scales as

$$\mathcal{O} \left(KJ \left[m + \sum_{d=1}^D f_d \right] n + KJ_u n^2 \right).$$

Thus, computational complexity is reduced by a power of m for the replacement of the exact Tikhonov solution with NAGD steps. Still, both versions have non-linear polynomial growth in computational complexity and thus, further computational reductions are required for scaling DR-CG-Net to signals of significantly higher dimension.

D. Network Parameters

Table II displays the number of parameters, i.e. unknowns, for DR-CG-Net and all ten compared deep learning-based methods for linear inverse problems. Note that the ratio

TABLE II: Parameter count for each compared deep learning method when reconstructing a 32×32 image from Radon transform measurements at 15 uniformly spaced angles.

Method	Parameters ($\times 10^5$)	Method	Parameters ($\times 10^5$)
ISTA DR-CG-Net	7.26	PGD DR-CG-Net	7.26
CG-Net	1.17	ISTA-Net ⁺	3.37
LPD	2.53	MADUN	29.7
LEARN ⁺⁺	12.0	FISTA-Net	0.75
iRadonMAP	8.33	iPiano-Net	19.3
FBPConvNet	7.09	ReconNet	7.30

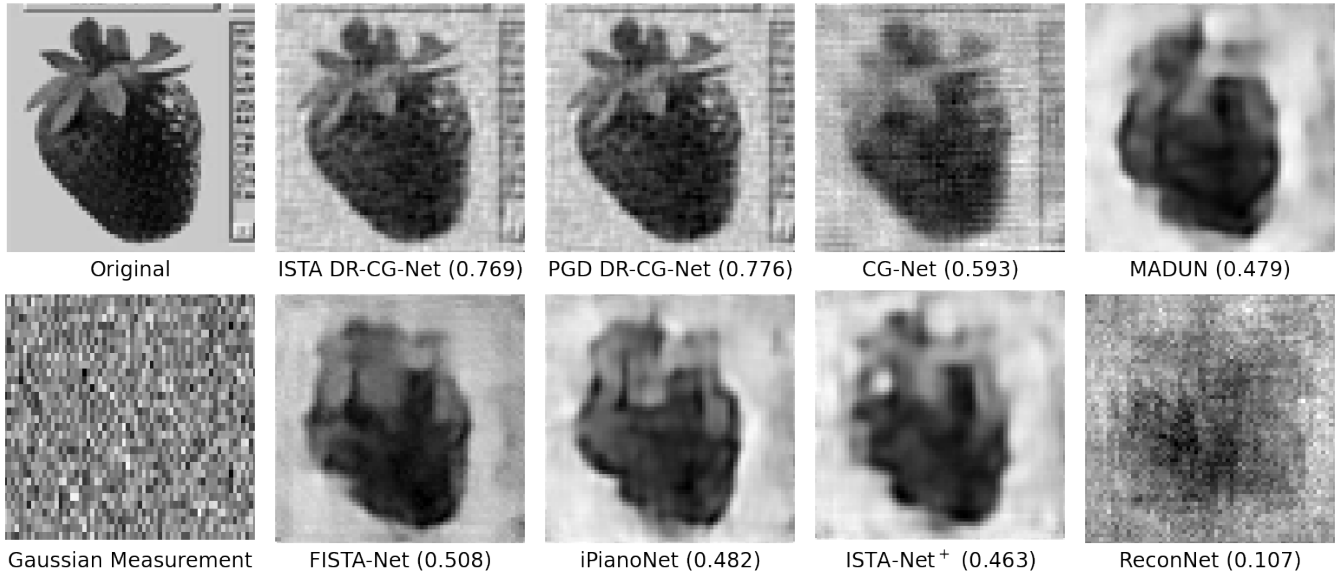


Fig. 6: Image reconstructions (SSIM) using our DR-CG-Net and six comparative deep learning methods on a 64×64 strawberry image after training on only 20 samples. Ψ = Gaussian matrix at 0.5 sampling ratio, Φ = discrete cosine transformation, and measurements have an SNR of 60dB. DR-CG-Net method performs best visually, particularly the leaf detail, and by SSIM.

of unknowns to data point measurements can be obtained by dividing each entry of Table II by the number of data points. For example, when training with 20 CIFAR10 images and 15 angle Radon transforms we use $20 \times (\text{image size} + \text{Radon transform size}) = 20 \times (1024 + 690) = 3.428 \times 10^4$ points of data, giving a ratio of unknowns to measurements of $7.26 \times 10^5 / (3.428 \times 10^4) \approx 21.2$ for DR-CG-Net. Instead, when training with 20 LoDoPaB-CT images and 60 angle Radon transforms, we have a ratio of unknowns to measurements of $7.26 \times 10^5 / (5.46 \times 10^5) \approx 1.33$ for DR-CG-Net. These ratios are on par with FBPCovNet and ReconNet that have a similar number of parameters to DR-CG-Net.

While the ratio of unknowns to measurements is high in low-training scenarios, our empirical results demonstrate that DR-CG-Net handles this situation well. In particular, we note that despite DR-CG-Net having a significantly greater ratio of unknowns to measurements than CG-Net, DR-CG-Net outperforms CG-Net when both are trained on small training datasets.

E. Refinement Block Study

Here, we investigate the impact that the refinement block, \mathcal{G} , has on the quality of the reconstructed signals produced by DR-CG-Net. To this end, we empirically evaluate two alternative formulations for DR-CG-Net where \mathcal{G} is removed before training (b.t.) and after training (a.t.) as shown in Table III. When \mathcal{G} is removed before training, a fresh DR-CG-Net is trained, as in the setup of Section V-B, with the C block now as output. Instead, when \mathcal{G} is removed after training, a trained DR-CG-Net from Section V-B is truncated to return the C block as output and no additional training is conducted.

For both instances of removing the refinement block, the reconstruction quality of DR-CG-Net remains significant indicating that the unrolled G-CG-LS portion of DR-CG-Net is

the core component in the superb reconstructions produced by DR-CG-Net. Additionally, higher noise, i.e. 40dB SNR, results in a larger discrepancy in the DR-CG-Net performance when the refinement block is or is not implemented as compared to the lower noise case. This suggests that the refinement block primarily denoises the estimated image from the unrolled G-CG-LS portion of DR-CG-Net.

TABLE III: Refinement block study for ISTA DR-CG-Net. Displayed is the average SSIM and PSNR for CIFAR10 image reconstructions from a Radon transform, at several different amounts of uniformly spaced angles, with a set SNR. **T** and **F** indicate if the refinement block is or is not used, respectively. Further, b.t. and a.t. denote if the refinement block is removed before or after training, respectively.

\mathcal{G}	(Angles, SNR)	Training Dataset Size					
		20		100		500	
		SSIM	PSNR	SSIM	PSNR	SSIM	PSNR
F b.t.	(15,60)	0.901	28.22	0.922	28.96	0.937	29.89
F a.t.		0.900	27.97	0.912	28.35	0.917	28.76
T		0.919	28.59	0.932	29.45	0.940	30.07
F b.t.	(15,40)	0.852	25.98	0.882	26.94	0.897	27.71
F a.t.		0.857	26.10	0.862	26.24	0.869	26.30
T		0.891	26.86	0.903	27.47	0.909	27.87
F b.t.	(10,60)	0.821	25.13	0.840	25.60	0.855	26.12
F a.t.		0.820	25.03	0.829	25.30	0.839	25.63
T		0.828	25.17	0.844	25.69	0.860	26.29
F b.t.	(10,40)	0.775	23.84	0.794	24.34	0.826	25.15
F a.t.		0.775	23.87	0.787	24.12	0.789	24.27
T		0.811	24.49	0.827	25.00	0.839	25.44

VI. CONCLUSION AND FUTURE WORK

Using a powerful learned CG class of densities, that subsume many commonly used priors in imaging and CS, this paper has presented new fundamental techniques for linear inverse problems. We developed a novel CG-based iterative estimation algorithm, named G-CG-LS, that allows for

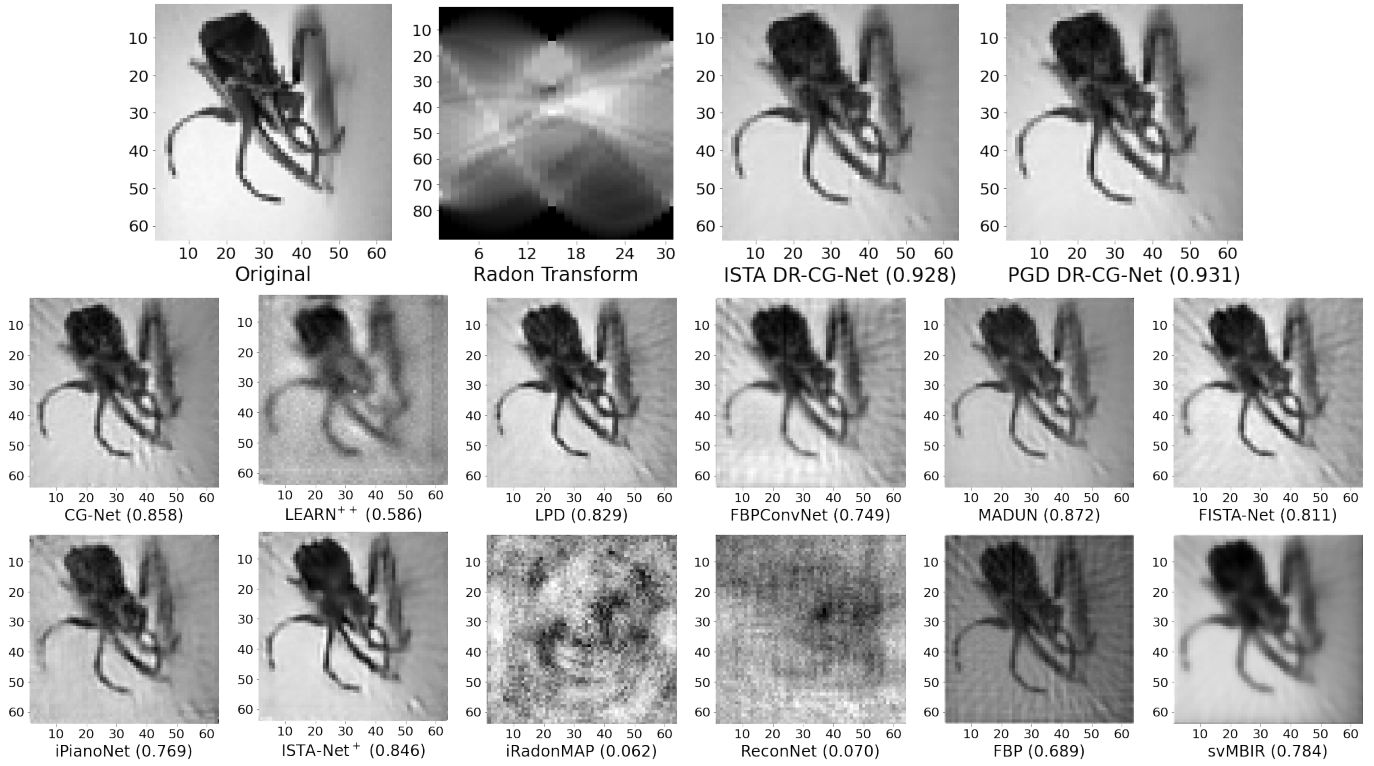


Fig. 7: Image reconstructions (SSIM) using our DR-CG-Nets, ten comparative deep learning methods, and two baseline iterative-based methods on a 64×64 spider image. The sensing matrix, Ψ , is a Radon transform at 30 uniformly spaced angles, $\Phi = I$, and each measurement has an SNR of 60dB. Our DR-CG-Net methods perform best visually and by SSIM.

problem-specific choices of the scale variable distribution by generalizing on prior CG-based methods. Applying algorithm unrolling to G-CG-LS, we constructed a novel CG-based deep neural network, named DR-CG-Net, that optimally learns the scale variable portion and the Gaussian covariance portion of the CG distribution. Hence, DR-CG-Net has the flexibility to learn the prior while constraining to the informative CG class of distributions.

We conducted a theoretical characterization of G-CG-LS and a fundamental numerical validation of DR-CG-Net in tomographic imaging and CS problems. Across multiple datasets, we empirically demonstrated that DR-CG-Net significantly outperforms competitive state-of-the-art deep learning-based methods in tomographic imaging and CS scenarios, especially in the difficult case of low-training. While CG-Net, which DR-CG-Net expands upon, is the closest comparative method in signal reconstruction quality for the low-training scenarios, CG-Net is still appreciably outperformed by DR-CG-Net both in estimated signal quality and in the computational time required to train and reconstruct a signal.

Leveraging the new foundations established in this paper, numerous opportunities for future investigation are illuminated including: analyzing the performance of DR-CG-Net on larger signal reconstructions, on data corrupted by different noise models, and for training with larger datasets. Studying each of these future objectives will provide greater insight into the practical, real-world applicability of our method.

We foresee the main complication in reconstructing larger

images to be hardware constraints in the memory required to store matrices for and calculate the Tikhonov solution. One workaround is replacing the Tikhonov solution with gradient descent steps, as we did for our 128×128 image results. While gradient descent steps only approximate the Tikhonov solution, we empirically showed that DR-CG-Net still successfully estimates images and outperforms all compared state-of-the-art approaches. For Radon transform measurements, A , in (1), is a sparse matrix that can be stored in a memory-efficient way (i.e. as a SparseTensor object in TensorFlow). Thus, with the development of a sparse linear solver through TensorFlow, only a slight modification of our code is necessary to efficiently deploy DR-CG-Net, with the exact Tikhonov solution, on larger images. Additionally, for Radon transform measurements, a matrix-free method, such as conjugate gradient, may be substituted to approximate the Tikhonov solution without constructing and storing the forward operator matrix. For CS applications, a common technique is to split larger images into disjoint blocks of small size and then measure and reconstruct the blocks separately [19, 43]; this strategy can be employed for future experimental evaluation of DR-CG-Net.

Another intriguing line of work is empirically studying DR-CG-Net, and each comparison deep learning method, for training and testing on a single category of images. The training and testing datasets employed in this paper contain images from multiple categories, e.g. CIFAR10 has 10 categories and CalTech101 has 101 categories, creating a significant statistical variability in the datasets. For some methods, such as FBP-

ConvNet, the statistical variability in the training and testing datasets can distort performance. As such, it would be of interest to observe if DR-CG-Net continues to provide state-of-the-art performance on single modal datasets or if other deep learning methods are better suited when homogeneity in the training and testing datasets is known upfront. Furthermore, it would be of interest to observe how DR-CG-Net and all the other deep learning methods generalize to images from alternative categories after training on a single category. We conjecture that DR-CG-Net will generalize well to images outside of the training class in a similar manner to how well it performs on the CalTech101 dataset.

Additional future work can explore alternative scale variable update methods, rather than PGD and ISTA, such as the alternating direction method of multipliers. The unrolled implementation for DR-CG-Net would require careful construction when using another scale variable update method but may provide performance benefits in reconstructed image quality. Furthermore, convergence properties of G-CG-LS with alternative scale variables update methods could be proven.

Finally, on the theoretical front, an open question emerging from our work is the formulation of a mathematical framework to explain the excellent generalization properties of DR-CG-Net in low-training scenarios. Approaches from statistical learning theory literature, such as constructing generalization error bounds, may provide insight into the superb low-training performance of DR-CG-Net.

VII. APPENDIX

First, the equivalence of a MAP estimate and our G-CG-LS estimate, which is proved in the supplementary material.

Proposition 5. *The optimum of cost function F in (3) is equivalent to a MAP estimate of \mathbf{z} and \mathbf{u} from (1).*

Second, an optimality condition defining a stationary point.

Definition 1. *Let $f : \mathcal{X} \rightarrow \mathbb{R}$ for convex \mathcal{X} . A point $\mathbf{x}^* \in \mathcal{X}$ is **stationary** if and only if for all $\mathbf{x} \in \mathcal{X}$ it holds that either*

- 1) *when f is differentiable, then $\langle \nabla f(\mathbf{x}^*), \mathbf{x} - \mathbf{x}^* \rangle \geq 0$ or*
- 2) *when f is convex, then there exists a \mathbf{d}^* in the subdifferential $\partial f(\mathbf{x}^*)$ such that $\langle \mathbf{d}^*, \mathbf{x} - \mathbf{x}^* \rangle \geq 0$.*

A. Projected Gradient Descent Bounds

Recall for a differentiable function $f : \mathcal{X} \rightarrow \mathbb{R}$ and initial point $\mathbf{x}_0 \in \mathcal{X}$ the PGD sequence $\{\mathbf{x}_k\}_{k=0}^\infty$ is defined as

$$\mathbf{x}_{k+1} = \mathcal{P}_{\mathcal{X}}(\mathbf{x}_k - \eta_{k+1} \nabla f(\mathbf{x}_k)),$$

where $\eta_{k+1} > 0$ a step size and $\mathcal{P}_{\mathcal{X}}$ a projection onto \mathcal{X} [37]. A backtracking linesearch in PGD chooses the largest $\eta_{k+1} \leq 1$ such that, for $\alpha \in (0, 1/2]$,

$$f(\mathbf{x}_{k+1}) \leq f(\mathbf{x}_k) - \alpha \langle \nabla f(\mathbf{x}_k), \mathbf{x}_k - \mathbf{x}_{k+1} \rangle. \quad (11)$$

Next, we bound the cost function change for a PGD step.

Lemma 1. *Let $f : \mathcal{X} \rightarrow \mathbb{R}$, for convex $\mathcal{X} \subseteq \mathbb{R}^d$, be a C^2 function with L -Lipschitz continuous gradient on a compact*

subset $\mathcal{S} \subseteq \mathcal{X}$. For $\mathbf{x}_0 \in \mathcal{S}$ and some positive constant c , the PGD sequence $\{\mathbf{x}_k\}_{k=0}^\infty$ with fixed step size $0 < \eta < 2/L$ or backtracking linesearch step size satisfies

$$f(\mathbf{x}_k) - f(\mathbf{x}_{k+1}) \geq c \|\mathbf{x}_{k+1} - \mathbf{x}_k\|_2^2. \quad (12)$$

Proof. From [49] $\mathcal{P}_{\mathcal{X}}(\mathbf{x})$ projects \mathbf{x} onto \mathcal{X} if and only if

$$\langle \mathbf{x} - \mathcal{P}_{\mathcal{X}}(\mathbf{x}), \mathbf{v} - \mathcal{P}_{\mathcal{X}}(\mathbf{x}) \rangle \leq 0 \quad \text{for all } \mathbf{v} \in \mathcal{X}. \quad (13)$$

In (13) take $\mathbf{x} = \mathbf{x}_k - \eta_{k+1} \nabla f(\mathbf{x}_k)$ and $\mathbf{v} = \mathbf{x}_k$, since $\mathcal{P}_{\mathcal{X}}(\mathbf{x}_k - \eta_{k+1} \nabla f(\mathbf{x}_k)) \equiv \mathbf{x}_{k+1}$ we have

$$\begin{aligned} 0 &\geq \langle \mathbf{x}_k - \eta_{k+1} \nabla f(\mathbf{x}_k) - \mathbf{x}_{k+1}, \mathbf{x}_k - \mathbf{x}_{k+1} \rangle \\ &= \|\Delta \mathbf{x}_k\|_2^2 - \eta_{k+1} \langle \nabla f(\mathbf{x}_k), \Delta \mathbf{x}_k \rangle \end{aligned}$$

for $\Delta \mathbf{x}_k := \mathbf{x}_k - \mathbf{x}_{k+1}$. Implying

$$-\langle \nabla f(\mathbf{x}_k), \Delta \mathbf{x}_k \rangle \leq -\|\Delta \mathbf{x}_k\|_2^2 / \eta_{k+1}. \quad (14)$$

As ∇f is L -Lipschitz we can bound the spectral radius of the Hessian of f by L . Combining this with Taylor's theorem to a second order remainder produces

$$f(\mathbf{x}_{k+1}) \leq f(\mathbf{x}_k) - \langle \nabla f(\mathbf{x}_k), \Delta \mathbf{x}_k \rangle + L \|\Delta \mathbf{x}_k\|_2^2 / 2 \quad (15)$$

$$\begin{aligned} &\leq f(\mathbf{x}_k) - \|\Delta \mathbf{x}_k\|_2^2 / \eta_{k+1} + L \|\Delta \mathbf{x}_k\|_2^2 / 2 \\ &= f(\mathbf{x}_k) - (1/\eta_{k+1} - L/2) \|\Delta \mathbf{x}_k\|_2^2 \end{aligned} \quad (16)$$

where the second inequality results from using (14). For fixed step sizes $\eta_{k+1} = \eta$ where $0 < \eta < 2/L$ we have (16) produces (12) with $c = \frac{1}{\eta} - \frac{L}{2}$.

Next, combining (14) and (15) again

$$f(\mathbf{x}_{k+1}) \leq f(\mathbf{x}_k) - (1 - L\eta_{k+1}/2) \langle \nabla f(\mathbf{x}_k), \Delta \mathbf{x}_k \rangle,$$

which implies the backtracking linesearch requirement (11) will hold when $\eta_{k+1} \leq 1/L$. Combining (11) and (14) with the fact that $\eta_{k+1} \leq 1$ produces (12) with $c = \alpha$. \square

Finally, we show that fixed points of PGD are stationary.

Lemma 2. *PGD fixed points are stationary.*

Proof. Let \mathbf{x}^* be a fixed point, i.e. $\mathbf{x}^* = \mathcal{P}(\mathbf{x}^* - \eta \nabla f(\mathbf{x}^*))$ for $\eta > 0$. Using (13) with $\mathbf{x} = \mathbf{x}^* - \eta \nabla f(\mathbf{x}^*)$ shows that \mathbf{x}^* satisfies 1) of Definition 1 and is a stationary point. \square

B. Iterative Shrinkage and Thresholding Algorithm Bounds

Recall [2] for a convex and differentiable function $f : \mathcal{X} \rightarrow \mathbb{R}$, a convex (possibly non-smooth) function $h : \mathcal{X} \rightarrow \mathbb{R}$, and $\mathbf{x}_0 \in \mathcal{X}$, the ISTA sequence $\{\mathbf{x}_k\}_{k=0}^\infty$ on $f(\mathbf{x}) + h(\mathbf{x})$ is

$$\mathbf{x}_{k+1} = \text{prox}_{\eta_{k+1}h}(\mathbf{x}_k - \eta_{k+1} \nabla f(\mathbf{x}_k)) \quad (17)$$

where $\eta_{k+1} > 0$ is a step size. As h can be non-smooth, a backtracking linesearch in ISTA only requires the gradient of f by choosing the largest $\eta_{k+1} \leq 1$ such that

$$f(\mathbf{x}_{k+1}) \leq f(\mathbf{x}_k) - \langle \nabla f(\mathbf{x}_k), \mathbf{x}_k - \mathbf{x}_{k+1} \rangle + \frac{\|\mathbf{x}_{k+1} - \mathbf{x}_k\|_2^2}{2\eta_k}. \quad (18)$$

Now we bound the cost function change for an ISTA step.

Lemma 3. *Let $f : \mathcal{X} \rightarrow \mathbb{R}$ be convex and have L -Lipschitz continuous gradient on a compact subset $\mathcal{S} \subseteq \mathcal{X}$. Let $h : \mathcal{X} \rightarrow$*

\mathbb{R} be convex. Then the ISTA sequence $\{\mathbf{x}_k\}_{k=1}^\infty$ on $r := f + h$ with fixed step size η , for $0 < \eta \leq 1/L$, or step size determined by a backtracking linesearch, satisfies

$$r(\mathbf{x}_k) - r(\mathbf{x}_{k+1}) \geq c \|\mathbf{x}_{k+1} - \mathbf{x}_k\|_2^2 \quad (19)$$

for some positive constant c .

Proof. Let $\mathbf{p}_\eta(\mathbf{v}) = \text{prox}_{\eta h}(\mathbf{v} - \eta \nabla f(\mathbf{v}))$ and define $\Delta \mathbf{v} := \mathbf{p}_\eta(\mathbf{v}) - \mathbf{v}$. Since f and h are convex, from [2] (Lemma 2.3) for any η such that

$$f(\mathbf{p}_\eta(\mathbf{v})) \leq f(\mathbf{v}) + \langle \nabla f(\mathbf{v}), \Delta \mathbf{v} \rangle + \|\Delta \mathbf{v}\|_2^2 / (2\eta) \quad (20)$$

it holds that

$$r(\mathbf{x}) - r(\mathbf{p}_\eta(\mathbf{v})) \geq \|\Delta \mathbf{v}\|_2^2 / (2\eta) + \langle \mathbf{v} - \mathbf{x}, \Delta \mathbf{v} \rangle / \eta. \quad (21)$$

As f has L -Lipschitz continuous gradient, then (20), and thus (21), holds for any $0 < \eta \leq 1/L$.

Let $\mathbf{x} = \mathbf{v} = \mathbf{x}_k$ then $\mathbf{p}_\eta(\mathbf{v}) = \mathbf{x}_{k+1}$ by (17). Hence, for fixed step size $\eta_{k+1} = \eta$, (21) produces (19) with $c = \frac{1}{2\eta}$. Next, when using a backtracking linesearch, observe for $0 < \eta_{k+1} \leq 1/L$ that (20) holds and implies the backtracking linesearch inequality (18). Combining (21) with the fact that $\eta_{k+1} \leq 1$ produces (19) with $c = 1/2$. \square

Lastly, we show that fixed points of ISTA are stationary.

Lemma 4. *Every ISTA mapping fixed point is stationary.*

Proof. Let \mathbf{x}^* be a fixed point, i.e. $\mathbf{x}^* = \text{prox}_{\eta h}(\mathbf{x}^* - \eta \nabla f(\mathbf{x}^*))$ for $\eta > 0$. By definition of the proximal operator \mathbf{x}^* satisfies 2) of Definition 1 and is a stationary point. \square

C. Proposition 1 Details

To prove Proposition 1 we use Lemma 1, Lemma 3, and the following Lemma about sublevel sets.

Lemma 5. *Let (\mathcal{A}_1) hold and (\mathcal{A}_2) or (\mathcal{A}_3) hold. The set*

$$S(\mathbf{u}_0, \mathbf{z}_0) = \{(\mathbf{u}, \mathbf{z}) \in \mathbb{R}^n \times \mathfrak{Z} : F(\mathbf{u}, \mathbf{z}) \leq F(\mathbf{u}_0, \mathbf{z}_0)\},$$

for $(\mathbf{u}_0, \mathbf{z}_0) \in \mathbb{R}^n \times \mathfrak{Z}$, is compact.

Proof. Both (\mathcal{A}_2) and (\mathcal{A}_3) imply F is continuous and so $S(\mathbf{u}_0, \mathbf{z}_0)$ is closed. By (\mathcal{A}_1) , for any $i = 1, 2, \dots, n$,

$$\lim_{u_i \rightarrow \pm\infty} F(\mathbf{u}, \mathbf{z}) \rightarrow \infty \quad \text{and} \quad \lim_{z_i \rightarrow \infty} F(\mathbf{u}, \mathbf{z}) \rightarrow \infty.$$

Hence $S(\mathbf{u}_0, \mathbf{z}_0)$ is bounded and thus is compact. \square

We now show $\{F(\mathbf{u}_k, \mathbf{z}_k)\}_{k=1}^\infty$ converges.

Proof of Proposition 1. Let $f(\mathbf{u}, \mathbf{z}) = \frac{1}{2} \|\mathbf{y} - A(\mathbf{z} \odot \mathbf{u})\|_2^2$, which is a C^2 function in \mathbf{z} . When (\mathcal{A}_3) holds, $F(\mathbf{u}, \mathbf{z})$ is also a C^2 function in \mathbf{z} . Thus, $H_{f;\mathbf{z}}(\mathbf{u}, \mathbf{z})$ and $H_{F;\mathbf{z}}(\mathbf{u}, \mathbf{z})$, the \mathbf{z} Hessians of f and F respectively, are continuous. Hence, $\|H_{f;\mathbf{z}}(\mathbf{u}, \mathbf{z})\|_2$ and $\|H_{F;\mathbf{z}}(\mathbf{u}, \mathbf{z})\|_2$ are also continuous.

Let $\text{ch}(S)$ denote the convex hull of a set S . By Lemma 5, $S(\mathbf{u}_0, \mathbf{z}_0)$ is compact and thus Carathéodary's Theorem implies $\text{ch}(S(\mathbf{u}_0, \mathbf{z}_0))$ is also compact. By the extreme value theorem $\|H_{f;\mathbf{z}}(\mathbf{u}, \mathbf{z})\|_2$ and $\|H_{F;\mathbf{z}}(\mathbf{u}, \mathbf{z})\|_2$ obtain a maximum on $\text{ch}(S(\mathbf{u}_0, \mathbf{z}_0))$. Therefore, by the mean value theorem f and F have Lipschitz continuous gradient on $\text{ch}(S(\mathbf{u}_0, \mathbf{z}_0))$ and thus on $S(\mathbf{u}_0, \mathbf{z}_0)$ as $S(\mathbf{u}_0, \mathbf{z}_0) \subseteq \text{ch}(S(\mathbf{u}_0, \mathbf{z}_0))$.

Hence, for PGD G-CG-LS when (\mathcal{A}_3) holds, Lemma 1 holds. Similarly, for ISTA G-CG-LS where (\mathcal{A}_2) holds, Lemma 3 (taking $r = \mathcal{R}$) holds. Consequently, for all $k \in \mathbb{N}$, any $j = 1, \dots, J$, and either PGD or ISTA G-CG-LS, we have

$$F(\mathbf{u}_{k-1}, \mathbf{z}_k^{(j-1)}) - F(\mathbf{u}_{k-1}, \mathbf{z}_k^{(j)}) \geq c \|\mathbf{z}_k^{(j)} - \mathbf{z}_k^{(j-1)}\|_2^2. \quad (22)$$

Then $F(\mathbf{u}_{k-1}, \mathbf{z}_{k-1}) \geq F(\mathbf{u}_{k-1}, \mathbf{z}_k) \geq F(\mathbf{u}_k, \mathbf{z}_k)$ holds for all $k \in \mathbb{N}$. Therefore, $\{F(\mathbf{u}_k, \mathbf{z}_k)\}_{k=1}^\infty$ is a monotonic decreasing sequence that is bounded below and thus converges. \square

D. Theorem 2 Details

Proving Theorem 2 uses Proposition 1, Lemma 2 and 4.

Proof of Theorem 2. Summing (22), from the Proposition 1 proof, over j , and using that $\mathbf{z}_k^{(0)} = \mathbf{z}_{k-1}$, $\mathbf{z}_k^{(J)} = \mathbf{z}_k$, and $F(\mathbf{u}_{k-1}, \mathbf{z}_k) \geq F(\mathbf{u}_k, \mathbf{z}_k)$ produces

$$F(\mathbf{u}_{k-1}, \mathbf{z}_{k-1}) - F(\mathbf{u}_k, \mathbf{z}_k) \geq c \sum_{j=1}^J \|\mathbf{z}_k^{(j)} - \mathbf{z}_k^{(j-1)}\|_2^2. \quad (23)$$

By Proposition 1, $\{F(\mathbf{u}_\ell, \mathbf{z}_\ell)\}_{\ell=1}^\infty$ converges and we let F^* be the limit point. Hence, summing (23) over $k \in \mathbb{N}$ and using that the left hand side of (23) is a telescoping sum we have

$$F(\mathbf{u}_0, \mathbf{z}_0) - F^* \geq c \sum_{k=1}^\infty \sum_{j=1}^J \|\mathbf{z}_k^{(j)} - \mathbf{z}_k^{(j-1)}\|_2^2. \quad (24)$$

Thus $\lim_{k \rightarrow \infty} \|\mathbf{z}_k^{(j)} - \mathbf{z}_k^{(j-1)}\|_2^2 \rightarrow 0$ for every $j = 1, 2, \dots, J$.

We make two remarks. First, note that for any real-valued sequence $\{x_k\}_{k=1}^\infty$ the Cauchy-Schwarz inequality implies $\sum_{j=1}^J x_j^2 \geq \frac{1}{J} \left(\sum_{j=1}^J x_j \right)^2$. Second, using a telescoping sum and the triangle inequality note that

$$\|\mathbf{z}_k - \mathbf{z}_{k-1}\|_2 = \left\| \sum_{j=1}^J (\mathbf{z}_k^{(j)} - \mathbf{z}_k^{(j-1)}) \right\|_2 \leq \sum_{j=1}^J \|\mathbf{z}_k^{(j)} - \mathbf{z}_k^{(j-1)}\|_2.$$

Combining these two notes and (24) produces

$$F(\mathbf{u}_0, \mathbf{z}_0) - F^* \geq \frac{c}{J} \sum_{k=1}^\infty \|\mathbf{z}_k - \mathbf{z}_{k-1}\|_2^2.$$

Hence, it also holds that $\lim_{k \rightarrow \infty} \|\mathbf{z}_k - \mathbf{z}_{k-1}\|_2^2 \rightarrow 0$. By continuity of the Tikhonov solution it similarly holds that $\lim_{k \rightarrow \infty} \|\mathbf{u}_k - \mathbf{u}_{k-1}\|_2^2 = \lim_{k \rightarrow \infty} \|\mathcal{T}(\mathbf{z}_k) - \mathcal{T}(\mathbf{z}_{k-1})\|_2^2 \rightarrow 0$.

Next, let $(\mathbf{u}^*, \mathbf{z}^*)$ be any limit point of $\{(\mathbf{u}_k, \mathbf{z}_k)\}_{k=1}^\infty$ and $\{(\mathbf{u}_{k_i}, \mathbf{z}_{k_i})\}_{i=1}^\infty$ the subsequence converging to $(\mathbf{u}^*, \mathbf{z}^*)$. By Lemma 1 and Lemma 3 the sequence of step sizes $\{\eta_{k_i}^{(1)}\}_{i=1}^\infty$ is bounded and thus there exists a convergent subsequence $\{\eta_{k_{i_\ell}}^{(1)}\}_{\ell=1}^\infty$. Let η^* be the limit point. As $\{(\mathbf{u}_{k_i}, \mathbf{z}_{k_i})\}_{i=1}^\infty$ converges every subsequence converges to the same limit point implying $\{(\mathbf{u}_{k_{i_\ell}}, \mathbf{z}_{k_{i_\ell}})\}_{\ell=1}^\infty$ converges to $(\mathbf{u}^*, \mathbf{z}^*)$. As $\lim_{k \rightarrow \infty} \|\mathbf{z}_k - \mathbf{z}_{k-1}\|_2^2 \rightarrow 0$ and $\lim_{k \rightarrow \infty} \|\mathbf{u}_k - \mathbf{u}_{k-1}\|_2^2 \rightarrow 0$ then $\{(\mathbf{u}_{k_{i_\ell}-1}, \mathbf{z}_{k_{i_\ell}-1})\}_{\ell=1}^\infty$ converges to $(\mathbf{u}^*, \mathbf{z}^*)$. Similarly, as $\lim_{k \rightarrow \infty} \|\mathbf{z}_k^{(j)} - \mathbf{z}_k^{(j-1)}\|_2^2 \rightarrow 0$ for every $j = 1, 2, \dots, J$ we have

$$\lim_{\ell \rightarrow \infty} \|\mathbf{z}_{k_{i_\ell}}^{(1)} - \mathbf{z}_{k_{i_\ell}}^{(0)}\|_2^2 = \lim_{\ell \rightarrow \infty} \|\mathbf{z}_{k_{i_\ell}}^{(1)} - \mathbf{z}_{k_{i_\ell}-1}\|_2^2 \rightarrow 0,$$

which implies $\{z_{k_{i_\ell}}^{(0)}\}_{\ell=1}^\infty$ and $\{z_{k_{i_\ell}}^{(1)}\}_{\ell=1}^\infty$ converge to z^* . In PGD G-CG-LS, by continuity of \mathcal{P}_3 [49] and $\nabla_z F$, observe

$$\lim_{\ell \rightarrow \infty} z_{k_{i_\ell}}^{(1)} = \lim_{\ell \rightarrow \infty} \mathcal{P}_3 \left(z_{k_{i_\ell}}^{(0)} - \eta_{k_{i_\ell}}^{(1)} \nabla_z F(u_{k_{i_\ell}-1}, z_{k_{i_\ell}}^{(0)}) \right) \\ z^* = \mathcal{P}_3(z^* - \eta^* \nabla_z F(u^*, z^*)).$$

Therefore, by Lemma 2 it holds that

$$\langle \nabla_z F(u^*, z^*), z - z^* \rangle \geq 0 \quad \text{for all } z \in \mathfrak{Z}. \quad (25)$$

In ISTA G-CG-LS, by continuity of the proximal operator [50]

$$\lim_{\ell \rightarrow \infty} z_{k_{i_\ell}}^{(1)} = \lim_{\ell \rightarrow \infty} \text{prox}_{\eta_{k_{i_\ell}}^{(1)} \mathcal{R}} \left(z_{k_{i_\ell}}^{(0)} - \eta_{k_{i_\ell}}^{(1)} A_{u_{k_{i_\ell}-1}}^T (A_{u_{k_{i_\ell}-1}} z_{k_{i_\ell}}^{(0)} - y) \right) \\ z^* = \text{prox}_{\eta^* \mathcal{R}} (z^* - \eta^* A_{u^*}^T (A_{u^*} z^* - y)).$$

Therefore, by Lemma 4, since $\partial_z F(u, z) = \nabla_z f(u, z) + \partial \mathcal{R}(z)$, there exists a $d^* \in \partial \mathcal{R}(z^*)$ such that

$$\langle \nabla_z f(u^*, z^*) + d^*, z - z^* \rangle \geq 0 \quad \text{for all } z \in \mathfrak{Z}. \quad (26)$$

As u^* is the global minimizer of $F(u, z^*)$ then

$$\langle \nabla_u F(u^*, z^*), u - u^* \rangle \geq 0 \quad \text{for all } u \in \mathbb{R}^n. \quad (27)$$

Adding together (25) and (27), for all $(u, z) \in \mathbb{R}^n \times \mathfrak{Z}$

$$\langle \nabla F(u^*, z^*), [u \ z]^T - [u^* \ z^*]^T \rangle \geq 0$$

and, similarly, adding together (26) and (27)

$$\langle \nabla f(u^*, z^*) + [P_u^{-1} u^* \ d^*]^T, [u \ z]^T - [u^* \ z^*]^T \rangle \geq 0.$$

Therefore (u^*, z^*) is a stationary point of $F(u, z)$. \square

E. Proposition 3 and Corollary 4 Details

Proving Proposition 3 uses Proposition 1 and Theorem 2.

Proof of Proposition 3. Let \mathcal{S} be the set of stationary points of (4) and $\{(u_k, z_k)\}_{k=0}^\infty$ the G-CG-LS sequence with limit point set \mathcal{L} . By Theorem 2, $\mathcal{L} \subseteq \mathcal{S}$ and $\{(u_k, z_k)\}_{k=0}^\infty$ satisfies $\lim_{k \rightarrow \infty} \|(u_{k+1}, z_{k+1}) - (u_k, z_k)\|_2 \rightarrow 0$. Hence, from [51] (Proposition 12.4.1) \mathcal{L} is connected. By Proposition 1, $\{F(u_k, z_k)\}_{k=1}^\infty$ converges to a value F^* . Thus, for every subsequence $\{(u_{k_i}, z_{k_i})\}_{i=1}^\infty$, $\{F(u_{k_i}, z_{k_i})\}_{i=1}^\infty$ converges to F^* . Hence (4) is constant on \mathcal{L} with value F^* . Finally, by definition $\{(u_k, z_k)\}_{k=0}^\infty$ converges to \mathcal{L} , which is closed [52]. \square

Lastly, we prove Corollary 4 using Proposition 3.

Proof of Corollary 4. By Proposition 3 the G-CG-LS sequence $\{(u_k, z_k)\}_{k=0}^\infty$ converges to its set of limit points \mathcal{L} which is connected. Since each stationary point is isolated then \mathcal{L} is a single point, to which $\{(u_k, z_k)\}_{k=0}^\infty$ converges. \square

VIII. ACKNOWLEDGEMENTS

We would like to thank all anonymous reviewers for their thoughtful comments that helped us improve this manuscript.

REFERENCES

- [1] I. Daubechies, M. Defrise, and C. De Mol, "An Iterative Thresholding Algorithm for Linear Inverse Problems with a Sparsity Constraint," *Commun. Pure Appl. Math.*, vol. 57, no. 11, pp. 1413–1457, Nov 2004.
- [2] A. Beck and M. Teboulle, "A Fast Iterative Shrinkage-Thresholding Algorithm for Linear Inverse Problems," *SIAM Journal on Imaging Sciences*, vol. 2, no. 1, pp. 183–202, Jan 2009.
- [3] S. Ji, Y. Xue, and L. Carin, "Bayesian Compressive Sensing," *IEEE Transactions on Signal Processing*, vol. 56, no. 6, pp. 2346–2356, 2008.
- [4] S. Foucart and H. Rauhut, *A Mathematical Introduction to Compressive Sensing*. Springer New York, 2013.
- [5] D. Needell and J. A. Tropp, "CoSaMP: Iterative signal recovery from incomplete and inaccurate samples," *Applied and Computational Harmonic Analysis*, vol. 26, no. 3, pp. 301–321, May 2009.
- [6] M. J. Wainwright and E. P. Simoncelli, "Scale Mixtures of Gaussians and the Statistics of Natural Images," in *Advances in Neural Information Processing Systems*, vol. 12, 1999, pp. 855–861.
- [7] M. J. Wainwright, E. P. Simoncelli, and A. S. Willsky, "Random Cascades on Wavelet Trees and Their Use in Analyzing and Modeling Natural Images," *Applied and Computational Harmonic Analysis*, vol. 11, no. 1, pp. 89–123, 2001.
- [8] C. Lyons, R. G. Raj, and M. Cheney, "A Compound Gaussian Least Squares Algorithm and Unrolled Network for Linear Inverse Problems," *IEEE Transactions on Signal Processing*, vol. 71, pp. 4303–4316, 2023.
- [9] Z. Chance, R. G. Raj, and D. J. Love, "Information-theoretic structure of multistatic radar imaging," in *IEEE RadarCon (RADAR)*, 2011, pp. 853–858.
- [10] Z. Idriss, R. G. Raj, and R. M. Narayanan, "Waveform Optimization for Multistatic Radar Imaging Using Mutual Information," *IEEE Transactions on Aerospace and Electronics Systems*, vol. 57, no. 4, pp. 2410–2425, Aug 2021.
- [11] K. Kulkarni, S. Lohit, P. Turaga, R. Kerviche, and A. Ashok, "ReconNet: Non-Iterative Reconstruction of Images From Compressively Sensed Measurements," in *Proceedings of the IEEE Conference on Computer Vision and Pattern Recognition*, 2016, pp. 449–458.
- [12] K. H. Jin, M. T. McCann, E. Froustey, and M. Unser, "Deep Convolutional Neural Network for Inverse Problems in Imaging," *IEEE Transactions on Image Processing*, vol. 26, no. 9, pp. 4509–4522, 2017.
- [13] J. He, Y. Wang, and J. Ma, "Radon Inversion via Deep Learning," *IEEE Transactions on Medical Imaging*, vol. 39, no. 6, pp. 2076–2087, 2020.
- [14] A. Bora, A. Jalal, E. Price, and A. G. Dimakis, "Compressed Sensing using Generative Models," in *Proceedings of the International Conference on Machine Learning*, vol. 70, 2017, pp. 537–546.
- [15] D. Liang, J. Cheng, Z. Ke, and L. Ying, "Deep Magnetic Resonance Image Reconstruction: Inverse Problems Meet Neural Networks," *IEEE Signal Processing Magazine*, vol. 37, no. 1, pp. 141–151, 2020.
- [16] G. Wang, J. C. Ye, and B. De Man, "Deep learning for tomographic image reconstruction," *Nature Machine Intelligence*, vol. 2, no. 12, pp. 737–748, Dec 2020.
- [17] K. Gregor and Y. LeCun, "Learning fast approximations of sparse coding," in *Proceedings of the 27th International Conference on Machine Learning*, 2010, pp. 399–406.
- [18] V. Monga, Y. Li, and Y. C. Eldar, "Algorithm Unrolling: Interpretable, efficient deep learning for signal and image processing," *IEEE Signal Processing Magazine*, vol. 38, no. 2, pp. 18–44, Mar 2021.
- [19] J. Song, B. Chen, and J. Zhang, "Memory-Augmented Deep Unrolling Network for Compressive Sensing," in *Proceedings of the 29th ACM International Conference on Multimedia*, Oct 2021, pp. 4249–4258.
- [20] J. Zhang and B. Ghanem, "ISTA-Net: Interpretable Optimization-Inspired Deep Network for Image Compressive Sensing," in *Proceedings of the IEEE Conference on Computer Vision and Pattern Recognition*, 2018, pp. 1828–1837.
- [21] J. Xiang, Y. Dong, and Y. Yang, "FISTA-Net: Learning a Fast Iterative Shrinkage Thresholding Network for Inverse Problems in Imaging," *IEEE Transactions on Medical Imaging*, vol. 40, no. 5, pp. 1329–1339, May 2021.
- [22] T. Meinhardt, M. Moller, C. Hazirbas, and D. Cremers, "Learning Proximal Operators: Using Denoising Networks for Regularizing Inverse Imaging Problems," in *Proceedings of the IEEE International Conference on Computer Vision*, 2017, pp. 1781–1790.
- [23] Y. Zhang, H. Chen, W. Xia, Y. Chen, B. Liu, Y. Liu, H. Sun, and J. Zhou, "LEARN++: Recurrent Dual-Domain Reconstruction Network for Compressed Sensing CT," *IEEE Transactions on Radiation and Plasma Medical Sciences*, 2022.

- [24] Y. Su and Q. Lian, "iPiano-Net: Nonconvex optimization inspired multi-scale reconstruction network for compressed sensing," *Signal Processing: Image Communication*, vol. 89, p. 115989, 2020.
- [25] J. Adler and O. Öktem, "Learned Primal-Dual Reconstruction," *IEEE Transactions on Medical Imaging*, vol. 37, no. 6, pp. 1322–1332, 2018.
- [26] C. Lyons, R. G. Raj, and M. Cheney, "CG-Net: A Compound Gaussian Prior Based Unrolled Imaging Network," in *2022 IEEE Asia-Pacific Signal and Information Processing Association Annual Summit and Conference*, 2022, pp. 623–629.
- [27] C. Lyons, R. G. Raj, and M. Cheney, "A Deep Compound Gaussian Regularized Unfolded Imaging Network," in *2022 56th Asilomar Conference on Signals, Systems, and Computers*, 2022, pp. 940–947.
- [28] M. Bertero, C. De Mol, and E. R. Pike, "Linear inverse problems with discrete data: II. Stability and regularisation," *Inverse Problems*, vol. 4, no. 3, pp. 573–594, Aug 1988.
- [29] R. G. Raj, "A hierarchical Bayesian-MAP approach to inverse problems in imaging," *Inverse Problems*, vol. 32, no. 7, p. 075003, Jul 2016.
- [30] J. McKay, R. G. Raj, and V. Monga, "Fast stochastic hierarchical Bayesian map for tomographic imaging," in *51st Asilomar Conference on Signals, Systems, and Computers*. IEEE, Oct 2017, pp. 223–227.
- [31] J. Portilla, V. Strela, M. J. Wainwright, and E. P. Simoncelli, "Image Denoising Using Scale Mixtures of Gaussians in the Wavelet Domain," *IEEE Transactions on Image Processing*, vol. 12, no. 11, pp. 1338–1351, Nov 2003.
- [32] T. Huang, W. Dong, X. Yuan, J. Wu, and G. Shi, "Deep Gaussian Scale Mixture Prior for Spectral Compressive Imaging," in *Proceedings of the IEEE/CVF Conference on Computer Vision and Pattern Recognition*, 2021, pp. 16 216–16 225.
- [33] I. Goodfellow, Y. Bengio, and A. Courville, *Deep Learning*. MIT press, 2016.
- [34] H. Zhao, O. Gallo, I. Frosio, and J. Kautz, "Loss Functions for Image Restoration With Neural Networks," *IEEE Transactions on Computational Imaging*, vol. 3, no. 1, pp. 47–57, Mar 2017.
- [35] S. J. Wright, "Coordinate descent algorithms," *Mathematical Programming*, vol. 151, no. 1, pp. 3–34, Jun 2015.
- [36] Y. Nesterov, "A method of solving a convex programming problem with convergence rate $O(1/k^2)$," in *Doklady Akademii Nauk*, vol. 269, no. 3. Russian Academy of Sciences, 1983, pp. 543–547.
- [37] D. P. Bertsekas, *Nonlinear Programming*. Athena Scientific, 2016.
- [38] Y. Xu and W. Yin, "A Block Coordinate Descent Method for Regularized Multiconvex Optimization with Applications to Nonnegative Tensor Factorization and Completion," *SIAM Journal on Imaging Sciences*, vol. 6, no. 3, pp. 1758–1789, 2013.
- [39] R. Murray, B. Swenson, and S. Kar, "Revisiting Normalized Gradient Descent: Fast Evasion of Saddle Points," *IEEE Transactions on Automatic Control*, vol. 64, no. 11, pp. 4818–4824, 2019.
- [40] D. P. Kingma and J. L. Ba, "Adam: A Method for Stochastic Optimization," *International Conference on Learning Representations*, 2015.
- [41] M. Abadi, P. Barham, J. Chen, Z. Chen, A. Davis, J. Dean, M. Devin, S. Ghemawat, G. Irving *et al.*, "TensorFlow: A System for Large-Scale Machine Learning," in *12th USENIX Symposium on Operating Systems Design and Implementation*, vol. 16, 2016, pp. 265–283.
- [42] X. Glorot and Y. Bengio, "Understanding the difficulty of training deep feedforward neural networks," in *Proceedings of the 13th International Conference on Artificial Intelligence and Statistics*. JMLR Workshop and Conference Proceedings, 2010, pp. 249–256.
- [43] J. Song, B. Chen, and J. Zhang, "Deep Memory-Augmented Proximal Unrolling Network for Compressive Sensing," *International Journal of Computer Vision*, vol. 131, no. 6, pp. 1477–1496, Jun 2023.
- [44] S. R. Deans, *The Radon Transform and Some of Its Applications*. Dover, 2007.
- [45] SVMBIR Development Team, "Super-Voxel Model Based Iterative Reconstruction (SVMBIR)," Software library available from <https://github.com/cabouman/svmbir>, 2020.
- [46] A. Krizhevsky, "Learning Multiple Layers of Features from Tiny Images," University of Toronto, Tech. Rep., 2009.
- [47] L. Fei-Fei, R. Fergus, and P. Perona, "Learning Generative Visual Models from Few Training Examples: An Incremental Bayesian Approach Tested on 101 Object Categories," in *Conference on Computer Vision and Pattern Recognition Workshop*, 2004, pp. 178–178.
- [48] J. Leuschner, M. Schmidt, D. O. Baguer, and P. Maass, "LoDoPaB-CT, a benchmark dataset for low-dose computed tomography reconstruction," *Scientific Data*, vol. 8, no. 1, p. 109, 2021.
- [49] W. Cheney and A. A. Goldstein, "Proximity Maps For Convex Sets," *Proceedings of the American Mathematical Society*, vol. 10, no. 3, pp. 448–450, 1959.
- [50] R. T. Rockafellar, "Monotone Operators and the Proximal Point Algorithm," *SIAM Journal on Control and Optimization*, vol. 14, no. 5, pp. 877–898, 1976.
- [51] K. Lange, *Optimization*. Springer Science & Business Media, 2013, vol. 95.
- [52] W. Rudin, *Principles of Mathematical Analysis*. McGraw Hill Education, 1953.

Supplementary Material: Deep Regularized Compound Gaussian Network for Solving Linear Inverse Problems

Carter Lyons^{1,2}, Raghu G. Raj¹, and Margaret Cheney²

¹U.S. Naval Research Laboratory, Washington, D.C.

²Colorado State University, Fort Collins, CO

I. ADDITIONAL DR-CG-NET NUMERICAL RESULTS

We provide additional simulation details and results for our deep regularized compound Gaussian network (DR-CG-Net). Please refer to the main manuscript for a summary of notation, nomenclature, and a more detailed description of the DR-CG-Net model. Recall that projected gradient descent (PGD) and iterative shrinkage and thresholding (ISTA) scale variable update methods are considered. Thus, PGD DR-CG-Net and ISTA DR-CG-Net, are two variants of DR-CG-Net that correspond to using a PGD or ISTA update of z , respectively.

We compare DR-CG-Net against ten state-of-the-art methods: (i) compound Gaussian network (CG-Net), (ii) memory augmented deep unfolding network (MADUN), (iii) ISTA-Net⁺, (iv) FISTA-Net, (v) iPiano-Net, (vi) ReconNet, (vii) LEARN⁺⁺, (viii) Learned Primal-Dual (LPD), (ix) FBPCConvNet, and (x) iRadonMAP. Note, LEARN⁺⁺, LPD, FBPCConvNet, and iRadonMAP are CT-specific reconstruction methods that rely on the structure of the CT sinogram measurements. On the other hand, MADUN, ISTA-Net⁺, FISTA-Net, iPiano-Net, and ReconNet are reconstruction methods with particular application in image compressive sensing. Furthermore, we remark that CG-Net, MADUN, ISTA-Net⁺, FISTA-Net, iPiano-Net, LEARN⁺⁺, and LPD are DNNs formed by algorithm unrolling while ReconNet, iRadonMAP, and FBPCConvNet are instead standard DNNs.

For data we use 32×32 CIFAR10 images, 64×64 CalTech101 images, and 128×128 LoDoPaB-CT images. Each image is converted to a single-channel grayscale image, scaled down by the maximum pixel value, and vectorized. We consider a Radon transform and random Gaussian matrix as measurement operators. To each measurement white noise is added producing noisy measurements, y , at a specified SNR.

A. DR-CG-Net Setup

Recall that for the unrolled iterations of each DR-CG-Net we set $(K, J) = (3, 4)$ and $(K, J) = (1, 24)$ for 32×32 images and 64×64 or 128×128 images, respectively. Additionally, each $\mathcal{V}_k^{(j)}$ is taken to be a CNN with depth $D = 8$. These network size parameters were chosen empirically such that the time to complete a signal reconstruction was reasonably quick while still producing excellent reconstructions on a

validation dataset. Every convolution uses a 3×3 kernel initialized according to the Glorot Uniform distribution with ReLU activation functions and $f_1 = \dots = f_7 = 32$ and $f_8 = 1$ filter channels.

We initialize each step size as $\delta_k^{(j)} = 1$, set $\gamma_{\max} = 1$, and fix $\epsilon = 10^{-4}$. Each u covariance matrix structure is initialized as a diagonal matrix with 0.1 or 10 on the diagonal for Radon transform or Gaussian measurements, respectively. Additionally, in the initial z estimate, we set $\mathcal{P}_{[0,b]^n} = \mathcal{P}_{[0,10]^n}$. For training datasets of size $N_s = 20$ and $N_s = 100$, we set a scaled identity u covariance matrix structure and a tridiagonal u covariance matrix structure is used for all other training datasets. Lastly, we train DR-CG-Net using the mean absolute error function with a learning rate of 10^{-4} for 2000 epochs.

B. Numerical Results

For each set of data, we train a PGD DR-CG-Net, ISTA DR-CG-Net, and each of the ten comparison methods. For CIFAR10 images, the training datasets consist of $N_s = 20, 100, 500, 1000$, and 2000 data samples and, after training, 8000 test data samples are provided to every network to assess its performance. For CalTech101 images, the training datasets consist of $N_s = 20$ samples and, after training, 200 test data samples are provided to every network. Average PSNR and SSIM quality metrics on the test dataset reconstructions are used to evaluate network performance where higher values of these metrics correspond to reconstructed images that more closely match the original.

We remark that every method was trained using early stopping. That is, as shown in Fig. 12, training was conducted until the model initially overfits as compared to a validation dataset. In doing so, we ensure every model is sufficiently trained while also not being over trained thereby presenting the best performance for each model given the provided set of training data.

Shown in Fig. 8 is the average PSNR quality over a set of test CIFAR10 image reconstructions from Radon transform measurements for ISTA DR-CG-Net and the comparison methods when each is trained on varying amounts of training data. We note that ReconNet, iRadonMAP, and some instances of FBPCConvNet perform significantly lower and are thus omitted from Fig. 8. Additionally, as PGD DR-CG-Net performed

arXiv:2311.17248v3 [eess.SP] 18 Mar 2024

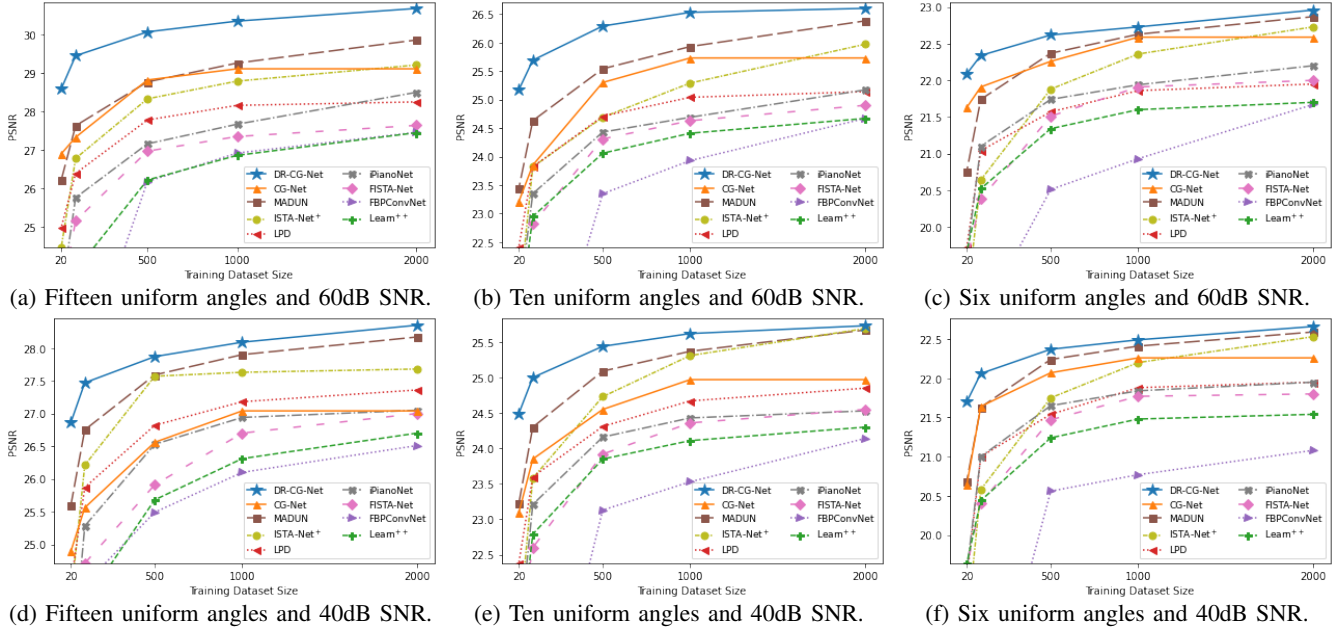


Fig. 8: Average test image reconstruction PSNR when varying the amount of CIFAR10 data in training nine machine learning-based image reconstruction methods. Here, the sensing matrices, Ψ , are a Radon transform at 15, 10, or 6 uniformly spaced angles, $\Phi = I$, and the measurement SNR is 60dB or 40dB. **Our DR-CG-Net method outperforms the compared prior art methods – for all measurement, noise, and training datasets except the smallest measurement and highest training dataset size – and does so appreciably in low training.**

nearly identically to ISTA DR-CG-Net, it too was omitted from Fig. 8. We can see from Fig. 8 that our DR-CG-Net outperforms all comparative methods in every training scenario, and does so significantly in the lowest training scenarios of 20 and 100 training samples.

Visual comparisons of all methods after training on 20 LoDoPaB-CT and CIFAR10 samples are provided in Fig. 9 and Fig. 10, respectively. In particular, Fig. 9 displays the estimates of a 128×128 scan from 76 uniformly spaced angle Radon transforms with 60dB SNR. Furthermore, Fig. 10 shows the reconstruction of a test plane image from Gaussian transform measurements at 0.5 sampling ratio with 60dB SNR. We observe both visually and quantitatively, by SSIM, that our PGD and ISTA DR-CG-Net methods perform comparably and outperform each prior art method.

Lastly, Fig. 11 provides average SSIM and PSNR performance on reconstructed CIFAR10 images after training on 20 samples. Each image is reconstructed from random Gaussian measurements at a 0.5, 0.3, or 0.1 sampling ratio with 60dB SNR. We remark that DR-CG-Net significantly outperforms each compared deep learning-based CS method in these low training CS experiments.

II. ALGEBRAIC PROOF MANIPULATIONS

A. Proposition 5 Details

Proof of Proposition 5. For random vector \mathbf{x} let $p_{\mathbf{x}}(\mathbf{x})$ be its probability density function and $p_{\mathbf{x}|\mathbf{v}}(\mathbf{x}|\mathbf{v})$ the conditional probability density given \mathbf{v} . Additionally, let $\mathcal{N}(\boldsymbol{\mu}, \Sigma)$ be a

multivariate normal distribution of mean $\boldsymbol{\mu}$ and covariance Σ . Observe

$$p_{\mathbf{y}|\mathbf{u}, \mathbf{z}}(\mathbf{y}|\mathbf{u}, \mathbf{z}) \sim \mathcal{N}(A(\mathbf{z} \odot \mathbf{u}), \sigma^2 I).$$

Since $\mathbf{u} \sim \mathcal{N}(\mathbf{0}, \Sigma_u)$ then using independence of \mathbf{u} and \mathbf{z} the MAP estimate of \mathbf{z} and \mathbf{u} from equation (1) is

$$\begin{aligned} & \arg \max_{\mathbf{u}, \mathbf{z}} p_{\mathbf{u}, \mathbf{z}|\mathbf{y}}(\mathbf{u}, \mathbf{z}|\mathbf{y}) \\ &= \arg \min_{\mathbf{u}, \mathbf{z}} -\ln(p_{\mathbf{y}|\mathbf{u}, \mathbf{z}}(\mathbf{y}|\mathbf{u}, \mathbf{z})) - \ln(p_{\mathbf{u}, \mathbf{z}}(\mathbf{u}, \mathbf{z})) \\ &= \arg \min_{\mathbf{u}, \mathbf{z}} -\ln(p_{\mathbf{y}|\mathbf{u}, \mathbf{z}}(\mathbf{y}|\mathbf{u}, \mathbf{z})) - \ln(p_{\mathbf{u}}(\mathbf{u})) - \ln(p_{\mathbf{z}}(\mathbf{z})) \\ &= \arg \min_{\mathbf{u}, \mathbf{z}} \frac{1}{2\sigma^2} \|\mathbf{y} - A(\mathbf{z} \odot \mathbf{u})\|_2^2 + \frac{1}{2} \mathbf{u}^T \Sigma_u^{-1} \mathbf{u} - \ln(p_{\mathbf{z}}(\mathbf{z})) \\ &= \arg \min_{\mathbf{u}, \mathbf{z}} \frac{1}{2} \|\mathbf{y} - A(\mathbf{z} \odot \mathbf{u})\|_2^2 + \frac{1}{2} \mathbf{u}^T P_u^{-1} \mathbf{u} + \mathcal{R}(\mathbf{z}) \end{aligned}$$

where $\mathcal{R}(\mathbf{z}) = -\sigma^2 \ln(p_{\mathbf{z}}(\mathbf{z}))$ and $P_u = \sigma^{-2} \Sigma_u$. \square

B. Improving the Tikhonov Solution

Here, we show the Tikhonov solution in equations (5) and (6) are equivalent. Observe using the Woodbury matrix identity

$$\begin{aligned} \mathcal{T}(\mathbf{z}) &= (A_{\mathbf{z}}^T A_{\mathbf{z}} + P_u^{-1})^{-1} A_{\mathbf{z}}^T \mathbf{y} \\ &= (P_u - P_u A_{\mathbf{z}}^T (I + A_{\mathbf{z}} P_u A_{\mathbf{z}}^T)^{-1} A_{\mathbf{z}} P_u) A_{\mathbf{z}}^T \mathbf{y} \\ &= (P_u A_{\mathbf{z}}^T - P_u A_{\mathbf{z}}^T (I + A_{\mathbf{z}} P_u A_{\mathbf{z}}^T)^{-1} A_{\mathbf{z}} P_u A_{\mathbf{z}}^T) \mathbf{y} \\ &= P_u A_{\mathbf{z}}^T (I - (I + A_{\mathbf{z}} P_u A_{\mathbf{z}}^T)^{-1} A_{\mathbf{z}} P_u A_{\mathbf{z}}^T) \mathbf{y} \\ &= P_u A_{\mathbf{z}}^T (I + A_{\mathbf{z}} P_u A_{\mathbf{z}}^T)^{-1} (I + A_{\mathbf{z}} P_u A_{\mathbf{z}}^T - A_{\mathbf{z}} P_u A_{\mathbf{z}}^T) \mathbf{y} \\ &= P_u A_{\mathbf{z}}^T (I + A_{\mathbf{z}} P_u A_{\mathbf{z}}^T)^{-1} \mathbf{y}. \end{aligned}$$

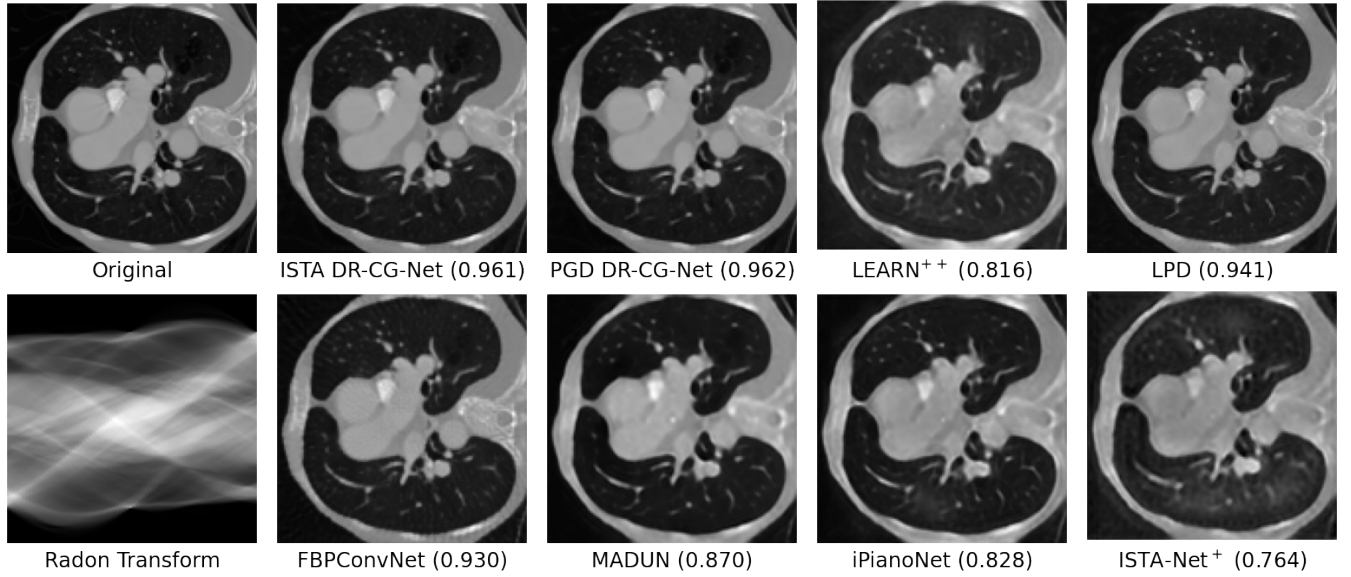


Fig. 9: Image reconstructions (SSIM) using our DR-CG-Net and six competitive deep learning methods on a 128×128 test scan after training with only 20 samples. The sensing matrix, Ψ , is a Radon transform at 76 uniformly spaced angles, $\Phi = I$, and each measurement has an SNR of 60dB. Our DR-CG-Net methods perform best visually and by SSIM.

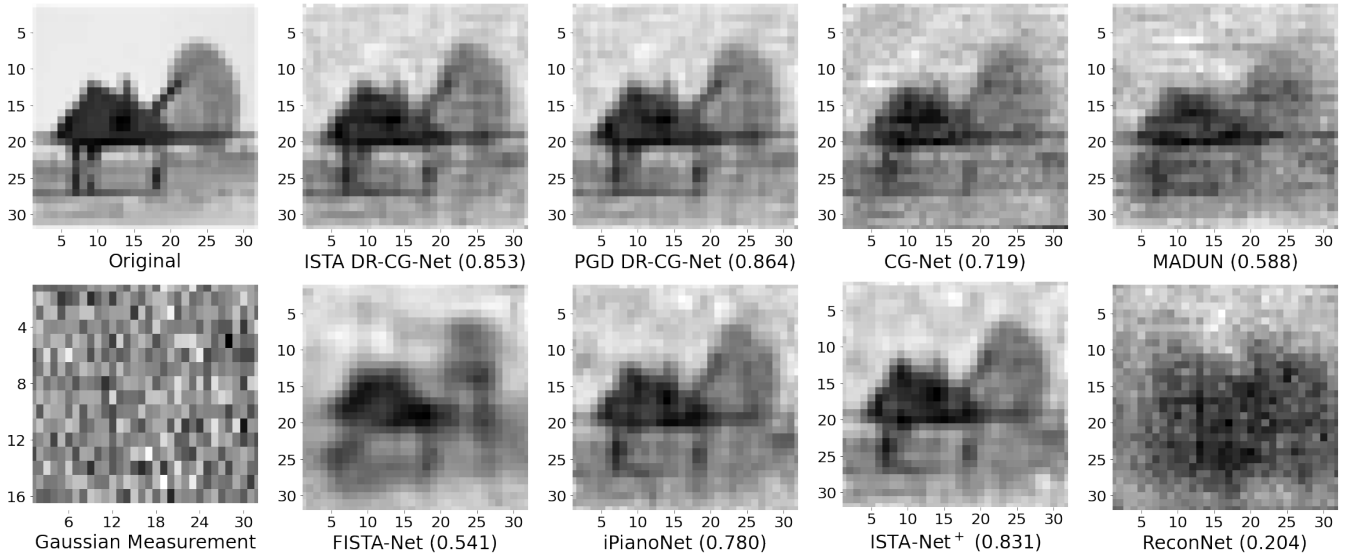


Fig. 10: Image reconstructions (SSIM) using our DR-CG-Net and six comparative deep learning methods on a 32×32 plane image after training on only 20 samples. The sensing matrix, Ψ , is a Gaussian matrix at 0.5 sampling ratio, $\Phi =$ discrete cosine transformation, and each measurement has an SNR of 60dB. Our DR-CG-Net methods perform best visually and by SSIM.

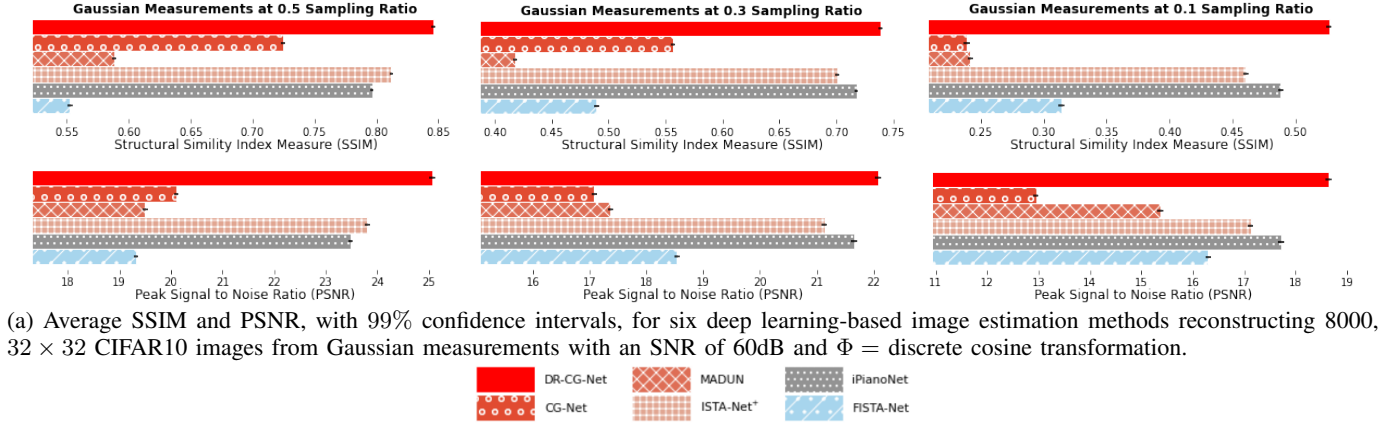


Fig. 11: Test image reconstruction quality for deep learning-based image estimation methods trained on only 20 samples. In all cases, our method, DR-CG-Net given by the top red bar, outperforms the other approaches.

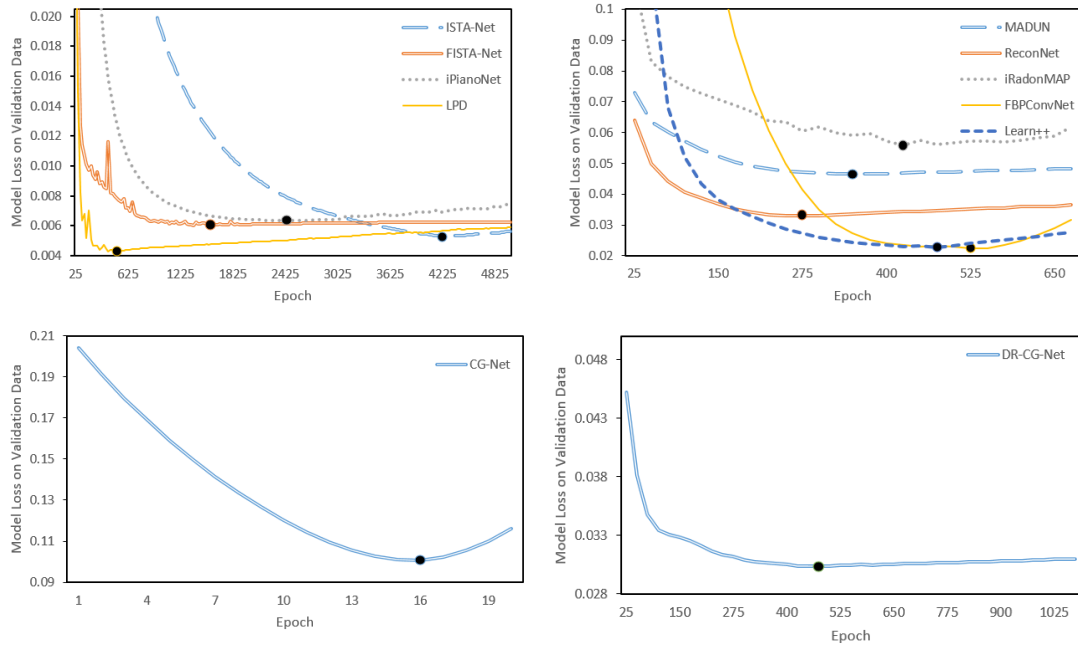


Fig. 12: Model loss curves on a validation dataset when training each deep learning-based method on Radon inversion from 15 uniformly spaced angles with 20 training samples. The point on each model's loss curve represents the epoch in which that model achieved its best loss on a validation dataset and overfits on subsequent epochs. Only these best loss epoch results are presented for each method. Note, for the plots above, CG-Net uses an SSIM loss function, MADUN and DR-CG-Net use a mean absolute error loss function, and all other methods use a mean square error loss function (possibly with some additional regularization). As the network loss functions are not equivalent, these plots do not contribute a comparison between the methods and only illustrate that each method is maximally trained for every supplied training dataset.